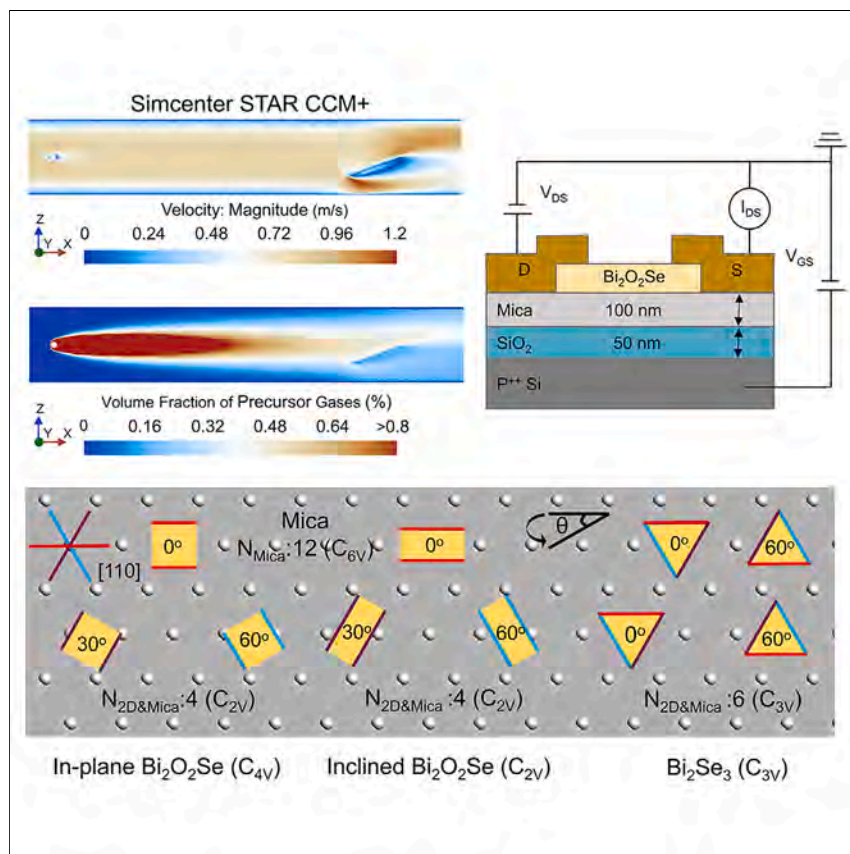


Article

Orientation-engineered 2D electronics on van der Waals dielectrics



Coordinated with Simcenter STAR CCM+ simulation, a hydromechanical strategy is initiated to achieve the aligned epitaxy of 2D materials on vdWs mica dielectrics. Combining density functional theory with Lagrange's group theorem, a criterion for how the oriented epitaxial growth of the 2D material on a 6-fold symmetric vdWs dielectric is quantitatively established. Moreover, the electrical characteristics of ultrathin as-grown Bi_2O_2Se -based FETs supported on their original epitaxial dielectric are evaluated at the device level.

Weijun Wang, Yuxuan Zhang, Wei Wang, ..., SenPo Yip, Weida Hu, Johnny C. Ho

wdhu@mail.sitp.ac.cn (W.H.)
johnnyho@cityu.edu.hk (J.C.H.)

Highlights

Designed a hydromechanical strategy for aligned 2D material synthesis

Quantitatively established the epitaxy relationship between 2D materials and vdWs dielectrics

Demonstrated high-performance devices with as-grown 2D materials/vdWs dielectrics



Development

Practical, real world, technological considerations and constraints

Wang et al., Matter 7, 1–14

June 5, 2024 © 2024 Elsevier Inc. All rights reserved.

<https://doi.org/10.1016/j.matt.2024.04.013>

Article

Orientation-engineered 2D electronics on van der Waals dielectrics

Weijun Wang,¹ Yuxuan Zhang,¹ Wei Wang,¹ Min Luo,² You Meng,¹ Bowen Li,¹ Yan Yan,¹ Di Yin,¹ Pengshan Xie,¹ Dengji Li,¹ Dong Chen,¹ Quan Quan,¹ SenPo Yip,³ Weida Hu,^{2,*} and Johnny C. Ho^{1,3,4,5,*}

SUMMARY

van der Waals (vdWs) dielectrics are widely used in nanoelectronics to preserve the intrinsic properties of two-dimensional (2D) semiconductors. However, achieving aligned growth of 2D semiconductors and their direct utilization on original vdWs epitaxial dielectrics to avoid disorders poses significant challenges. Here, a hydromechanical strategy for aligned epitaxy of 2D materials on naturally occurring vdWs mica dielectrics is developed. By combining density functional theory with Lagrange's group theorem, a quantitative criterion for 2D material epitaxy on 6-fold symmetric vdWs dielectrics is established. Moreover, the as-grown ultrathin Bi₂O₂Se-channeled field-effect transistor, with a hybrid dielectric layer, achieves a superior current on/off ratio (1.4×10^7) and high carrier mobility ($22.4 \text{ cm}^2 \text{ V}^{-1} \text{ S}^{-1}$) by directly integrating as-grown 2D materials/vdWs dielectrics. This work provides a powerful methodological platform for aligned 2D material synthesis, alignment direction prediction, and intrinsic property investigation, laying the foundation for advanced electronics on as-grown 2D materials/vdWs dielectrics.

INTRODUCTION

Batch fabrication of advanced two-dimensional (2D) field-effect transistors (FETs) necessitates the synthesis of high-quality 2D films, which is commonly accomplished by aligned coalescence of 2D material islands on specific substrates.^{1–3} However, the as-grown 2D films via the mainstream chemical vapor deposition (CVD) method are generally coalesced by enormous misoriented 2D material islands and may be meticulously detached from the original substrates onto proposed dielectrics for further device fabrication.^{4,5} Such processes can separately cause grain-boundary-induced disorders and surrounding disorders from chemical adsorbates or neighboring dielectrics, degrading the 2D material's intrinsic properties,^{3,6} such as carrier mobility and gate controllability. Compared to the 2D FETs based on conventional oxide dielectrics (such as SiO₂),⁷ the devices integrated with van der Waals (vdWs) dielectrics exhibit improved mobility and better switching stability,^{8,9} attributable to their atomically flat surfaces that are free of dangling-bond-induced disorders. Thus, achieving aligned growth of 2D materials and directly using them on their original vdWs epitaxial dielectrics to avoid disorders is being pursued with purposefully engineered off-cut angles toward future 2D nanoelectronics.^{10,11} Regrettably, achieving non-destructive manipulation of as-grown 2D materials with vdWs dielectrics, e.g., h-BN,¹² Sb₂O₃,^{13,14} etc., is currently challenging, hindering the direct integration of as-grown 2D materials on their original vdWs dielectrics.

PROGRESS AND POTENTIAL

Empowered by device miniaturization approaching the physical limits, 2D materials emerge as virtuosos, significantly influencing the trajectory of electronics in the post-Moore era. Leveraged by the hydromechanical strategy, 2D materials with preferential orientations on van der Waals (vdWs) dielectrics can be synthesized, facilitating the direct utilization of as-grown 2D materials/vdWs dielectrics at the device level to minimize disorder-induced performance degradation. Additionally, the establishment of the quantitative criterion for the epitaxy relationship with vdWs dielectrics can be aptly viewed as a measure of our understanding and can guide experimental decisions effectively. This work introduces a powerful methodology platform for synthesizing aligned 2D materials, predicting alignment directions, and preserving their intrinsic properties, holding substantial technological implications for unlocking the transformative potential of 2D materials.

Fortunately, the recent discovery of a naturally occurring vdWs dielectric, muscovite mica, has shed light on exploring those above challenging 2D nanoelectronic issues. Except for the dangling-bond-free surface that facilitates the aligned growth of various 2D materials,^{15–18} the mica dielectric provides rich redundancy of being precisely manipulated to desired thicknesses, owing to the relatively weak interlayer interaction.¹⁹ Also, it has a dielectric constant of 6.4–9.3,²⁰ nearly twice that of the conventional SiO₂ and h-BN, making it applicable for effective gate control and high-speed switching even down to a few atomic layers thick.^{3,21} Besides, mica with a large band gap (5.1 eV),²² high dielectric strength (0.1–1 V/nm),²³ and superior stability can make it an excellent dielectric layer, suitable for high electric fields and high-temperature harsh environments.^{24,25} In this regard, relying on vdWs mica dielectrics to develop advanced techniques for achieving aligned synthesis of 2D materials and direct utilization of as-grown 2D materials/vdWs dielectrics are fundamentally feasible and of great significance.

Herein, a hydromechanical strategy for achieving the aligned epitaxy of 2D materials on vdWs mica dielectrics, coordinated with Simcenter STAR CCM+ simulation, is first developed for the promising high-quality synthesis of large-scale 2D films via the coalescence process. In order to gain further insights into the epitaxial relationship between the 2D material and the 6-fold vdWs dielectric, we perform a systematic theoretical analysis by combining the density functional theory (DFT) calculation with Lagrange's group theorem. After that, an unreported criterion for how the epitaxial growth of the 2D material on a 6-fold symmetric vdWs dielectric is established. Moreover, a reproducible technique for high-precision manipulation of as-grown 2D materials on their original vdWs mica dielectric is initiated, while the electrical characteristics of ultrathin as-grown Bi₂O₂Se-based FETs supported on its original vdWs epitaxial substrate are evaluated at the device level.

RESULTS AND DISCUSSION

Aligned fabrication of the 2D materials

Figure 1A depicts a conventional CVD setup with a horizontally positioned growth substrate. As indicated by the carrier gas flow, prolonged precursor transport reduces the control over precursor concentration and growth temperature,^{26–28} resulting in non-uniform deposition of various Bi–O–Se products (Figure 1B), including in-plane Bi₂O₂Se, inclined Bi₂O₂Se, and Bi₂Se₃ nanoflakes, respectively. Disordered epitaxial growth on mica is observed for each product (Figure S1), owing to the poor controllability over the precursor transport process and growth temperature. In contrast, as shown in Figure 1C, different compositions can be controllably synthesized by regulating the growth temperature and the precursor weight ratio in the hydromechanics-based CVD system (Note S1), where the growth substrate is inclinedly placed in the CVD system (Figure S2). Figures 1D–1F show the optical microscope images of as-grown 2D products on the tilted mica with an angle of around 20°, demonstrating significantly better thickness uniformity and flake orientation in the modified CVD system. Remarkably, the results show that the in-plane and inclined Bi₂O₂Se crystals show three equivalent but different alignment angles on the mica substrate, while only two different orientations are observed for synthesizing 2D Bi₂Se₃ (detailed explanations will be provided later to investigate the intimate interplay between the 2D material and the mica substrate). A series of unique epitaxy characteristics for different 2D products, including orientations and morphology evolution, are observed (Figures S3–S9), showing the great potential of the hydro-mechanical synthesis strategy in the controllable synthesis of many other 2D materials.

¹Department of Materials Science and Engineering, City University of Hong Kong, Kowloon 999077, Hong Kong SAR, China

²State Key Laboratory of Infrared Physics, Shanghai Institute of Technical Physics, Chinese Academy of Sciences, Shanghai 200083, China

³Institute for Materials Chemistry and Engineering, Kyushu University, Fukuoka 816-8580, Japan

⁴State Key Laboratory of Terahertz and Millimeter Waves, City University of Hong Kong, Kowloon 999077, Hong Kong SAR, China

⁵Lead contact

*Correspondence: wdu@mail.sitp.ac.cn (W.H.), johnnyho@cityu.edu.hk (J.C.H.)

<https://doi.org/10.1016/j.matt.2024.04.013>

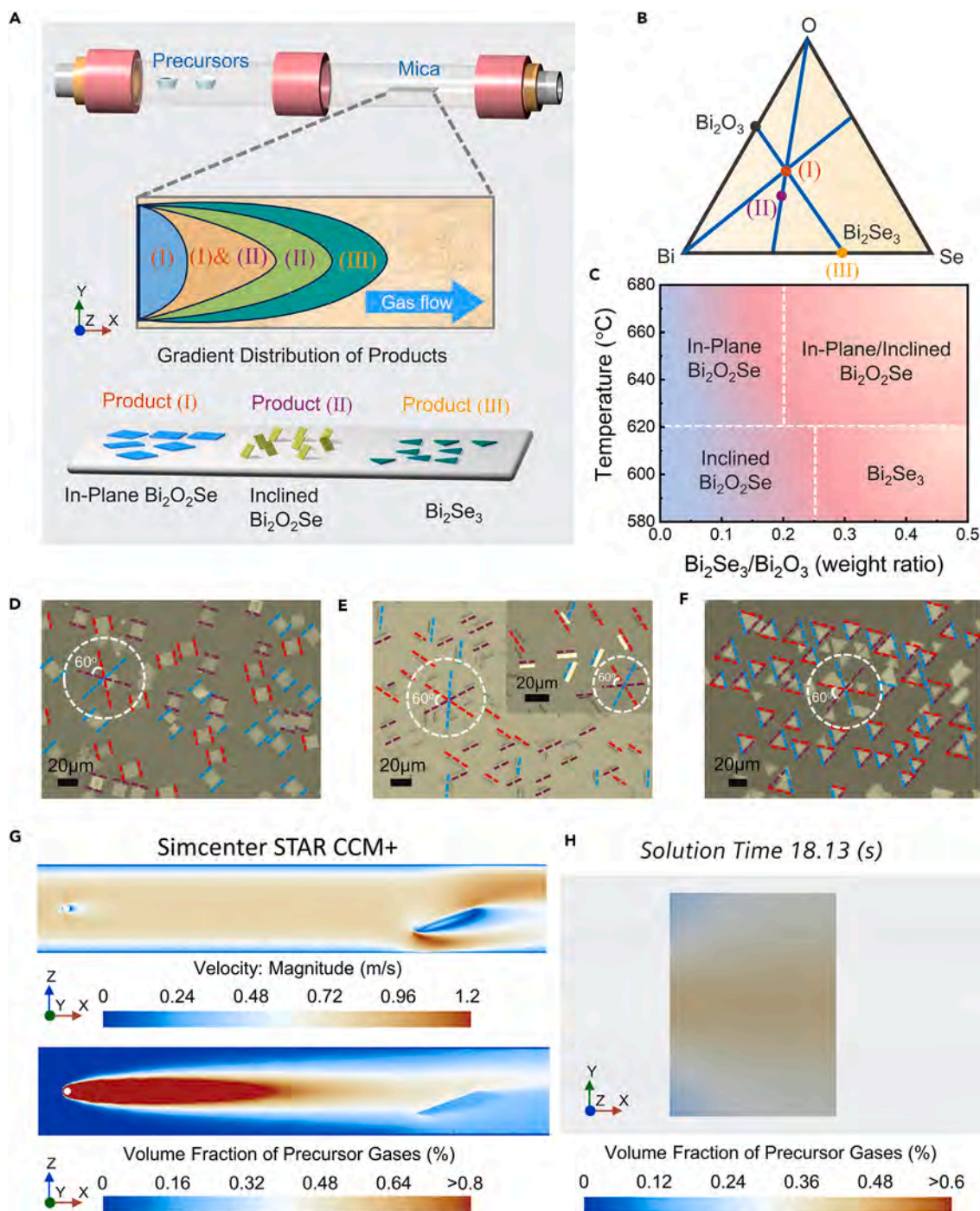


Figure 1. Hydromechanical strategy for aligned 2D material growth

(A) Schematic illustration of a conventional CVD system exhibiting the spatial sectioning of the growth substrate for (I) in-plane $\text{Bi}_2\text{O}_2\text{Se}$, (II) inclined $\text{Bi}_2\text{O}_2\text{Se}$, and (III) Bi_2Se_3 , respectively.

(B) Schematic representation of the Bi–O–Se ternary phase diagram.

(C) Summary of the Bi–O–Se products via regulating the temperatures and weight ratios of Bi_2Se_3 and Bi_2O_3 precursors.

(D–F) Optical microscope images of the well-orientated single-crystalline 2D islands along the high-symmetry direction. The crystallographic orientations of 2D material flakes are positioned in red, blue, and purple colors, respectively. Compared to the conventional CVD synthesis system (Figure S1), the hydrodynamics system demonstrates excellent controllability by yielding a specific single product without misorientation, showcasing its superiority.

Figure 1. Continued

(G) Simulated distribution of the carrier gas velocity (top) and the precursor concentration field (bottom) using Simcenter STAR CCM+ software for a hydromechanical CVD system.

(H) Simulated precursor concentration (~4% on average) on the top surface of the substrate at equilibrium with a solution time of 18.13 s.

It is essential to mention that although enormous research efforts have been devoted to $\text{Bi}_2\text{O}_2\text{Se}$ synthesis, this is the first report on the preferentially aligned growth of in-plane $\text{Bi}_2\text{O}_2\text{Se}$ nanoflakes on a substrate. A series of Simcenter STAR CCM+ simulations are performed for the conventional and hydrodynamic systems, keeping all other growth parameters constant, such as growth temperature, pressure, etc., to semiquantitatively compare their controllability of precursor transport (Figures S10–S12). The simulations highlight the significance of flow rate and precursor concentration across the growth substrate in a CVD reactor, providing strong evidence for robustly achieving the aligned growth of 2D materials in the hydrodynamics system. Figures 1G and 1H show the simulated result of carrier gas velocity and precursor concentration with the tilted angle of 20° and a solution time of 17.17 s, respectively. The result indicates that both gas flow velocity and precursor concentration near the mica substrate are effectively regulated since the tilted mica substrate (length \times width = 2×1.8 cm) can serve as a “valve” owing to the limited tube size (1 inch). More importantly, a lower precursor concentration dissipation is obtained for the hydrodynamic CVD system, compared to the conventional CVD system, with respect to the point source, demonstrating better controllability of the vapor precursor by simply regulating the valve angle. The above simulation results support our experimental observations and highlight the importance of deliberate process management to achieve a controllable synthesis of 2D materials in the CVD method by manipulating process parameters and reactor geometry.

Characteristics of the aligned 2D materials

The morphology and crystal structure of the 2D Bi–O–Se products are then investigated by a combination of experimental techniques. The atomic force microscopy (AFM) images of the 2D Bi–O–Se products are shown in Figures 2A–2C, revealing a clean and atomically flat surface topography with root-mean-square surface roughness of 5.08, 5.12, and 5.25 Å, respectively, within the area of $2 \times 2 \mu\text{m}$. Adopting the hydrodynamic strategy, the 2D Bi–O–Se products exhibit significantly improved controllability, with characteristic average thicknesses of ~ 7.2 nm for in-plane $\text{Bi}_2\text{O}_2\text{Se}$, ~ 20.9 nm for tilted $\text{Bi}_2\text{O}_2\text{Se}$, and ~ 7.1 nm for Bi_2Se_3 (Figures 2D–2F). Figure 2G exhibits that X-ray diffraction (XRD) measurements of in-plane $\text{Bi}_2\text{O}_2\text{Se}$,²⁹ inclined $\text{Bi}_2\text{O}_2\text{Se}$,³⁰ and Bi_2Se_3 ³¹ are well aligned with the previous works. Notably, the tilted $\text{Bi}_2\text{O}_2\text{Se}$ shows an additional (013) peak in the XRD measurements corresponding to the (013) crystal planes from the cross-sectional scanning transmission electron microscope images via focused ion beam sectioning.³⁰ The unmarked diffraction peaks originated from the pristine mica substrate match well with the standard XRD card PDF no. 16-0344 (Figure S13). X-ray photoelectron spectroscopy (XPS) reveals the chemical bonding states of Bi and Se for the in-plane/flat $\text{Bi}_2\text{O}_2\text{Se}$ and Bi_2Se_3 (Figure S14), and all the resolved peaks are consistent with the composition of previous works.^{32,33} The inclined $\text{Bi}_2\text{O}_2\text{Se}$ flakes are converted into flat ones for XPS measurements through proper ultrasonication since the XPS instrument can only analyze ~ 5 – 10 nm of the top surface,³⁴ making the signal intensity of inclined samples too weak for identification. Figures 2H and 2I display the related Raman spectra and optical analysis of each 2D product, which are well-aligned with their characteristic vibration peaks.^{30,35–37} Compared to in-plane or flat $\text{Bi}_2\text{O}_2\text{Se}$ flakes, a relatively large redshift of the A_{1g} peak for the inclined $\text{Bi}_2\text{O}_2\text{Se}$ is observed, which could be attributed to the inharmonicity of lattice vibrations.³⁸ (Note S2) The above

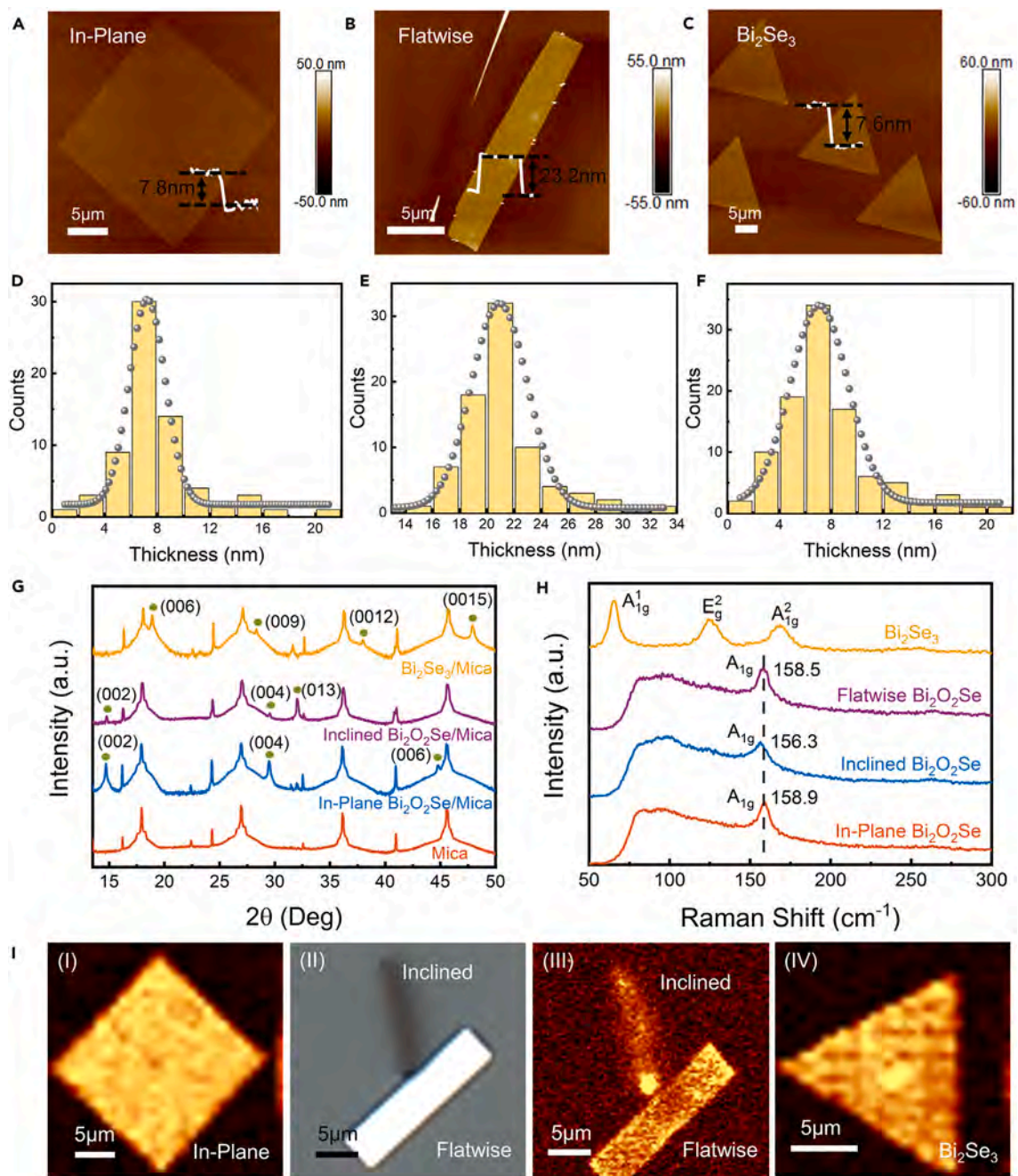


Figure 2. Characterization of the aligned 2D materials

(A–C) AFM measurements of 2D Bi–O–Se flakes with feature thicknesses of 7.8 (in-plane $\text{Bi}_2\text{O}_2\text{Se}$), 23.2 (inclined $\text{Bi}_2\text{O}_2\text{Se}$), and 7.6 nm (Bi_2Se_3), respectively.

(D–F) Average thickness distribution of the well-aligned Bi–O–Se flakes on mica substrate: in-plane $\text{Bi}_2\text{O}_2\text{Se}$ (~ 7.2 nm), inclined $\text{Bi}_2\text{O}_2\text{Se}$ (~ 20.9 nm), and Bi_2Se_3 flakes (~ 7.1 nm), respectively.

(G) XRD patterns of the pristine mica substrate and as-grown 2D Bi–O–Se flakes on mica substrates.

(H) Raman spectra of different 2D Bi–O–Se products on mica substrates. Meanwhile, flatwise $\text{Bi}_2\text{O}_2\text{Se}$ flakes refer to the inclined $\text{Bi}_2\text{O}_2\text{Se}$ flakes after 2 s of ultrasound.

(I) Optical measurements of the related 2D flakes. (I) Raman mapping of the as-grown $\text{Bi}_2\text{O}_2\text{Se}$ A_{1g} peak. (II and III) Optical microscope image and corresponding Raman mapping of $\text{Bi}_2\text{O}_2\text{Se}$ A_{1g} peak for the inclined and flat $\text{Bi}_2\text{O}_2\text{Se}$, respectively. (IV) Raman mapping of the as-grown Bi_2Se_3 A_{1g} peak.

analyses demonstrate that our 2D products synthesized by hydrodynamic strategy via the CVD method are of high quality with excellent uniformity, stoichiometry, crystallinity, etc.

Insight into the epitaxy relationship with vdWs dielectrics

Experimental observations indicate that the alignment of a 2D material on the mica substrate is synergistically influenced by the symmetries of the material itself and the underlying substrate. Thus, a comprehensive theory on 2D materials epitaxy, capable of predicting the alignment of various 2D products on mica substrates, is highly desirable as an experimental design guideline for large-scale 2D film synthesis. However, no general theory exists to explain the epitaxial relationship between different 2D materials on mica. Thanks to the weak bonding between the potassium (K) ions and aluminosilicate layers, vdWs mica dielectrics possess a perfect cleavage parallel to {001} planes,³⁹ which is intrinsically favorable for the lateral migration of precursor atoms and epitaxial growth of 2D materials.⁴⁰ The {001} cleavage planes, consisting of the K ions, with an ideal surface, possess a 6-fold rotational symmetry (C_6) (Figure S15), and the alignment of 2D materials with self-passivated edges on mica substrate is dominated by the weak vdWs forces.^{41,42} In such scenery, the interaction between 2D materials and mica {001} planes is required to reveal the alignment of 2D materials on mica by utilizing the periodic boundary condition models. Previous studies have shown that 2D materials (edges of graphene, h-BN, and transition-metal dichalcogenides [TMDCs]) tend to align their high-symmetry directions with those of their substrates, such as the $\langle 110 \rangle$ directions of Cu (111),⁴³ $\langle 11-20 \rangle$ of h-BN⁴⁴, and (0001) planes of Al_2O_3 .⁴⁵ This rule is consistent with our experimental observations on the epitaxial growth of in-plane $\text{Bi}_2\text{O}_2\text{Se}$, inclined $\text{Bi}_2\text{O}_2\text{Se}$, and Bi_2Se_3 on mica substrates (Figures 1D–1F), as well as being in perfect agreement with many experimental observations on 2D materials' growth on the vdWs mica dielectrics known up to now (Table S1).

To verify the assumption that a 2D material tends to align its high-symmetry direction with the high-symmetry direction of the mica surface, comprehensive DFT calculations are conducted based on our well-aligned 2D materials synthesis. Figures 3A–3C exhibit the schematic models of our 2D materials clusters aligning along the high-symmetry directions of the mica dielectric for the related DFT calculations. In the calculations, various angles between different 2D material clusters regarding vdWs mica dielectrics are modeled to ensure the accuracy of the calculations (Figures S16–S18). Detailed methods for calculations are provided in the experimental procedures. Figure 3D shows the binding energy of different 2D material clusters on a mica substrate as a function of the alignment angle between the self-passivated edges of 2D materials and the high-symmetry $\langle 110 \rangle$ direction of the mica {001} surface. These results show that the system's overall energy maintains the lowest value when the self-passivated edges of the 2D materials follow the high-symmetry direction of the neighboring vdWs substrate. Although we calculate very limited epitaxial systems of 2D materials on mica, the above results allow us to summarize the rule for the alignment of an arbitrary 2D material on mica, i.e., a high-symmetry direction of the 2D island prefers to align along a high-symmetry direction of the mica substrate.

With the principle that determines the alignment of an arbitrary 2D material on a mica substrate established, we will further discuss how the symmetries of both the substrate and the 2D material interact in the epitaxial growth. Considering a 2D material with a G_{2D} symmetry group placed on a 6-fold mica substrate (G_{Mica}), the symmetry group of the system, $G_{2D\&\text{Mica}}$, must be a subgroup of either G_{2D} or G_{Mica} because the alignment of the 2D material and the substrate remains unaffected by any symmetry operation of $G_{2D\&\text{Mica}}$. As derived in Note S3, the number of

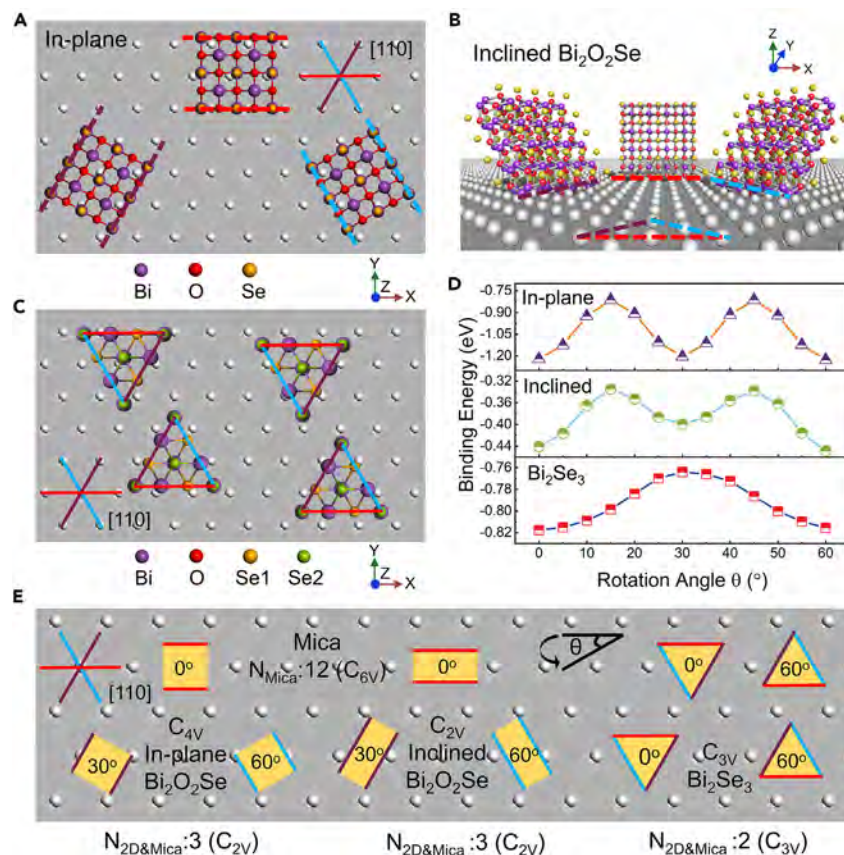


Figure 3. Study on the epitaxy relationship with vdWs dielectrics

(A–C) Schematic model of 2D materials clusters aligning along the high-symmetry direction of the mica dielectric.

(D) The calculated binding energies of the 2D materials cluster on the mica surface as a function of the alignment angle (θ) between a high-symmetry direction of 2D materials and a high-symmetry mica surface.

(E) The number of equivalent but distinct alignments of our experimental 2D products on the mica substrate. The symmetry groups of the mica substrate, 2D materials, and the system of the 2D island on mica are provided. The number of symmetry operations of the mica substrate and the whole system are N_{Mica} and $N_{2D\&Mica}$, respectively. Consistent with our experimental observations, these 2D products, including in-plane $\text{Bi}_2\text{O}_2\text{Se}$, inclined $\text{Bi}_2\text{O}_2\text{Se}$, and Bi_2Se_3 , exhibit 3, 3, and 2 equivalent but different orientations, respectively.

equivalent but distinct directions of a 2D material on mica {001} surfaces, defined as N_E , can be computed using the following formula, derived from Lagrange's theorem of the group theory^{46,47}:

$$N_E = \frac{|G_{\text{Mica}}|}{|G_{2D\&Mica}|},$$

where $|G_{\text{Sub}}|$ and $|G_{2D\&Mica}|$ are the numbers of distinct symmetry operations of G_{Sub} and $G_{2D\&Mica}$, respectively. According to the abovementioned principle of arbitrary 2D materials on mica, a high-symmetry edge of a 2D material preferably aligned along a high-symmetry direction of the mica substrate, the symmetry group of the whole system, $G_{2D\&Mica}$, must be the largest subgroup of both G_{Mica} and G_{2D} . Given all possible combinations of the symmetries of the 2D material and the mica substrate, the number of equivalent but distinct alignments of various 2D materials on mica {001} surfaces are summarized (Table 1). Consequently, according to our

Table 1. Summary of the number of equivalents

G_{2D}	C_{6V}	C_{4V}	C_{3V}	C_{2V}
G_{Mica}	C_{6V}	C_{6V}	C_{6V}	C_{6V}
$G_{2D\&Mica}$	C_{6V}	C_{2V}	C_{3V}	C_{2V}
$ G_{Mica} $	12	12	12	12
$ G_{2D\&Mica} $	12	4	6	4
N_E	1	3	2	3

The number of equivalent but different orientations of a 2D material on a mica substrate is based on the interplay between their symmetries.

experimental observation and theoretical analysis (Figure 3E), we believe that the N_E for most 2D materials synthesized on mica can be reasonably predicted, providing a desirable experimental design guideline before the general synthesis of 2D materials on the vdWs mica dielectric.

High-precision manipulation of the vdWs dielectric

After demonstrating the superiority of the oriented growth of 2D materials, device-level implementations based on as-grown 2D materials/vdWs dielectrics to reveal the “true” properties of as-grown 2D materials are further explored, utilizing vdWs mica/SiO₂ as the hybrid dielectric layers. Figure 4A illustrates the device fabrication process of the FETs, in which a high-fidelity transfer method is developed by utilizing the thermal releasing tape to assist in the fabrication of hybrid mica/SiO₂ dielectric layers. Figure 4B depicts the schematic of the backgated FET, and its optical and AFM images demonstrate the thicknesses of the Bi₂O₂Se layer and mica dielectric layer with atomic-scale flatness as 3.4 and ~100 nm, respectively (Figure S19). It is worth mentioning that the thickness of the as-grown Bi₂O₂Se/vdWs mica dielectric heterostructures is controlled by the exfoliation time with blue tape before thermally releasing onto SiO₂. As shown in Figure 4C, the corresponding transfer curves of the device on a logarithmic scale reveal a record-high current on/off ratio of 1.4×10^7 at a relatively small source/drain bias of $V_{DS} = 20$ mV. Figure 4D exhibits the linear output curves of the device at V_{GS} sweeping from -15 to 15 V, demonstrating the ohmic contact between the Bi₂O₂Se semiconductor channel and Au electrodes.

Compared to many state-of-the-art 2D-material-channeled FETs integrated with various dielectrics (Figure 4E), our Bi₂O₂Se-based FETs with hybrid mica/SiO₂ gate dielectrics show high mobility of 22.3 ± 1.2 cm² V⁻¹ S⁻¹ for a channel thickness down to 3.4 nm of about 6 layers (Figures S20 and S21), which is superior or comparable to the most widely investigated non-vdWs dielectrics, e.g., Al₂O₃, SiO₂, HfO₂, etc. (Table S2). This high carrier mobility of the ultrathin Bi₂O₂Se flake not only demonstrates the high quality of our CVD-grown ultrathin 2D Bi₂O₂Se materials but also shows the low interface trap density and coulomb impurity concentration as compared to the other device techniques (Figures S22–S24). Figure 4F gives the high current on/off ratio (1.4×10^7) of our Bi₂O₂Se FETs, which is significantly better or comparable to many promisingly 2D materials, including TMDCs, black phosphorus (BP), β -Ga₂O₃, etc., demonstrating the excellent coupling of as-grown Bi₂O₂Se flakes on the transferable hybrid dielectrics. By leveraging the as-grown Bi₂O₂Se on its original vdWs epitaxial dielectric, the FETs exhibit improved performance attributes and mitigate the detrimental effects that can arise from additional device fabrication steps, showing their superiority in reducing the performance degradation of the CVD-grown 2D semiconductors (Figure S25). Considering the high transparency, excellent flexibility, and suitable insulating properties of mica, this research lays the foundation for potential device-level studies on the transferable dielectric of mica, e.g., flexible transparent electronics.

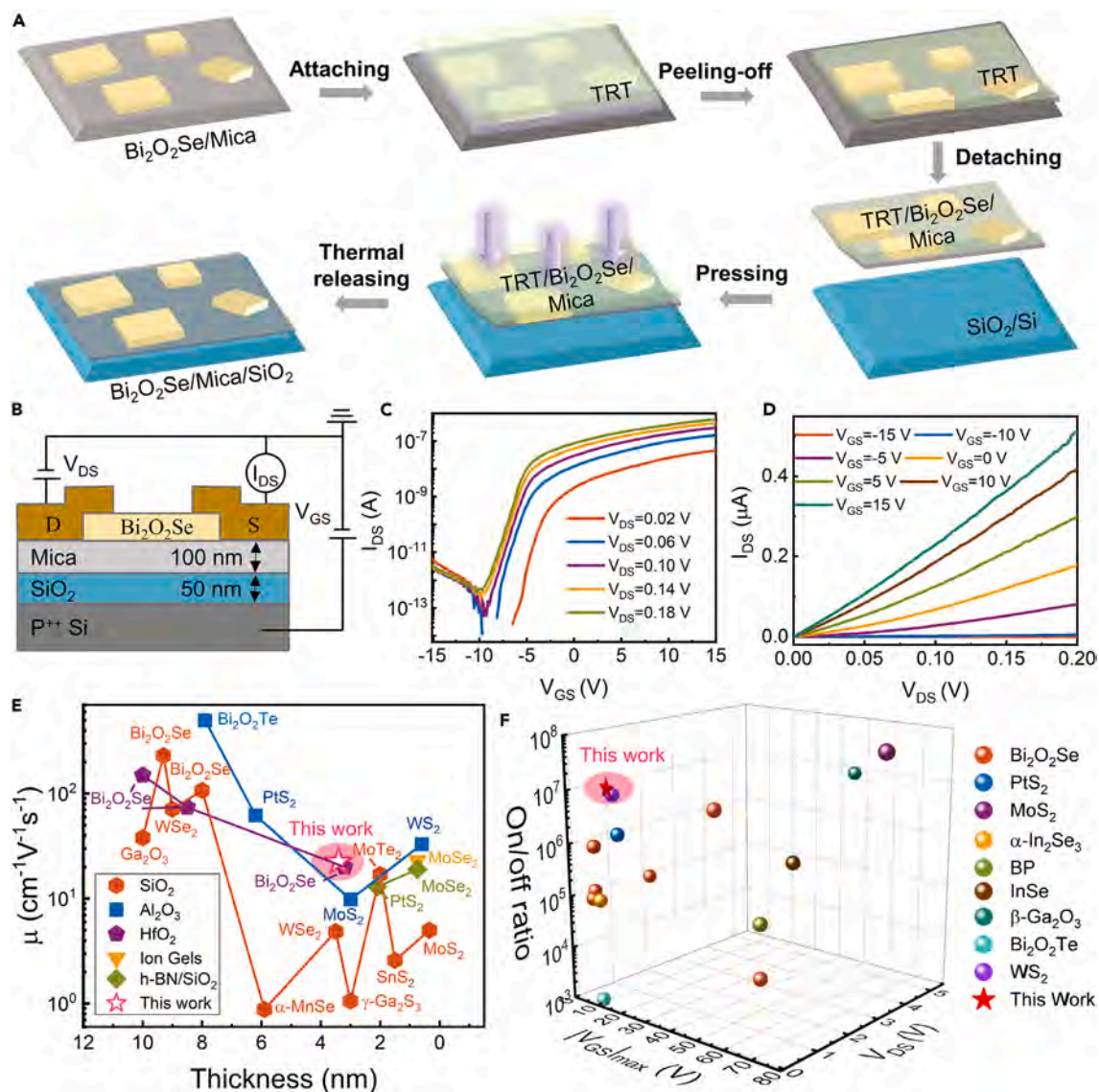


Figure 4. Device fabrication and performance evaluations

(A) Device fabrication process of the Bi₂O₂Se FETs using mica/SiO₂ as hybrid dielectric layers via a high-fidelity transfer method assisted by the thermal releasing tape (TRT).

(B) Schematic illustration of the back-gated FETs where the Bi₂O₂Se semiconductor and mica/SiO₂ hybrid layer are used as the transistor channel and gate dielectric, respectively.

(C) Transfer curves of the mica-based Bi₂O₂Se FETs as V_{DS} increases from 0.02–0.18 V, revealing typical n-type characteristics with a current on/off ratio of 1.4×10^7 .

(D) Output characteristics of the Bi₂O₂Se FET as V_{GS} increases from –15 to 15 V.

(E) Mobility of our Bi₂O₂Se-based FETs with the hybrid mica/SiO₂ gate dielectric compared to other state-of-the-art 2D FETs integrated with various dielectrics.^{48–65}

(F) On/off ratio of the device at a relatively small bias of V_{DS} = 0.02 V as gate voltages sweep from –15 to 15 V, and the performance comparison with the state-of-the-art 2D FETs based on distinct categories of 2D materials, e.g., TMDCs, BP, β-Ga₂O₃, etc.^{30,48,57,60–70}

Conclusions

In summary, we investigate the aligned epitaxy of 2D materials and develop a method for the high-fidelity manipulation of as-grown 2D materials on the vdWs mica dielectric at the device level. The aligned epitaxy of distinct CVD-grown 2D materials is realized by adopting the hydromechanical strategy. Simcenter STAR

CCM+ simulation is employed to understand the enhanced precursor controllability during the CVD synthesis. In addition, the insight into the epitaxy relationship between our 2D products and vdWs mica dielectrics is uncovered by DFT calculations, demonstrating the energy-favorable directions of 2D clusters on mica dielectrics. Specifically, combined with Lagrange's theorem of the group theory, the number of equivalent but different directions of a 2D material on mica is first established, potentially applicable to many other 2D epitaxy systems. More importantly, detailed electrical device characterization is performed for the high-fidelity manipulation of the as-grown Bi₂O₂Se-based device with hybrid dielectrics, exhibiting a record high current on/off ratio of 1.4×10^7 and excellent carrier mobility of $22.4 \text{ cm}^2 \text{ V}^{-1} \text{ S}^{-1}$. Overall, this work provides a powerful methodology platform for synthesizing the aligned 2D materials, predicting the alignment direction, evaluating their intrinsic properties, and laying the foundation for probing device functionalities, e.g., flexible transparent electronics.

EXPERIMENTAL PROCEDURES

Resource availability

Lead contact

Further information and requests for resources and reagents should be directed to and will be fulfilled by the lead contact, Johnny C. Ho (johnnyho@cityu.edu.hk).

Materials availability

This study did not generate new unique reagents.

Data and code availability

Any additional information required to reanalyze the data reported in this paper is available from the [lead contact](#) upon request.

MATERIALS SYNTHESIS AND CHARACTERIZATION

Bi₂O₂Se flakes were synthesized by the CVD method using Bi₂Se₃ (Aldrich, 99.99%) and Bi₂O₃ (Thermo Scientific, 98%) powders as the precursors.^{71,72} The quartz boat of the Bi₂O₃ side was put in the center of the heating zone, and the mica substrate was placed at a proper downstream position accordingly. The furnace was heated to 635°C–650°C with a ramping time of 10 min and a holding time of 10–25 min under ~ 124 torr. Ahead of the heating process, the furnace tube was flushed with high-purity argon gas to thoroughly exhaust the atmospheric moisture and oxygen. After high-temperature deposition, the furnace was naturally cooled to room temperature. The topological morphologies of the materials were characterized by optical and atomic force microscopes (Dimension Icon, Bruker). Raman spectra were collected by a confocal microscope spectrometer (Alpha 300R, WITec).

Simcenter STAR CCM+ simulation

As the flow velocity in the tubular furnace remains relatively flat, a laminar flow model coupled with dilute material transfer modules was selected to simplify the numerical computation for mass transport in the CVD systems. The detailed models for the related Simcenter STAR CCM+ simulation are shown in [Figure S26](#). Except for the basic geometries of the two systems, other key parameters, e.g., pressure, carrier gas, etc., were consistent with the experimental condition provided in the [materials synthesis and characterization](#) section. It is worth noting that the precursor with a volume fraction of precursor gases (1%) was viewed as a continuous point source diffusion model (which is denoted as a normalized unit concentration). A balanced concentration distribution of the precursor vapor on growth substrates was obtained using the computational fluid dynamics solver.

DFT calculations of the binding energies

The DFT calculations were performed with the Vienna Ab-initio Simulation Package code with the full-potential projected augmented wave formalism.^{73,74} The generalized gradient approximation of the Perdew-Burke-Ernzerhof functional was used to describe the exchange and correlation functions.⁷⁵ The structure was relaxed until the atomic force was less than 0.01 eV \AA^{-1} , and the self-consistent calculation was terminated when the energy converged to 10^{-4} eV . A 2×2 unit cell of mica and a 2×2 unit cell of $\text{Bi}_2\text{O}_2\text{Se}$ or Bi_2Se_3 were constructed to match each other. To eliminate the perturbation from neighboring slabs, a vacuum layer of 20 \AA was used. The vdWs interaction between matched layers was considered by the DFT-D3 method of Grimme with a zero-damping function.⁷⁶ The cutoff energy for the plane-wave expansion was set to 450 eV , and a k-point mesh of $3 \times 3 \times 1$ was employed to sample the Brillouin zone.

To separately calculate the interaction between 2D products (in-plane $\text{Bi}_2\text{O}_2\text{Se}$, inclined $\text{Bi}_2\text{O}_2\text{Se}$, and Bi_2Se_3 nanoflakes), different pristine clusters with their typical geometry shapes were stacked onto a mica (001) surface under periodic boundary conditions and with different alignment angles (5° per step). During the geometry optimization, the top atomic layer of the K metal slab was fixed, as the edges of the clusters are generally self-passivated. The binding energy between the calculated 2D materials and the mica substrate is defined as

$$E_b = E_{\text{total}} - E_{2\text{D}} - E_{\text{mica}},$$

where E_{total} , $E_{2\text{D}}$, and E_{mica} are the energies of the whole system, the 2D materials layer, and the mica substrate, respectively.

Device fabrication and evaluation

For the back-gated FETs, the as-grown $\text{Bi}_2\text{O}_2\text{Se}$ flakes were detached from mica and transferred to the desired dielectric substrate by a poly(methyl methacrylate) (PMMA)-assisted wet-transfer method (Figure S13). The Au electrodes were patterned by electron-beam lithography and thermally evaporated with a thickness of 40 nm . The electronic performance was characterized by a semiconductor analyzer (Agilent 4155C) and probe station.

SUPPLEMENTAL INFORMATION

Supplemental information can be found online at <https://doi.org/10.1016/j.matt.2024.04.013>.

ACKNOWLEDGMENTS

This research was financially supported by a fellowship award from the Research Grants Council of the Hong Kong Special Administrative Region, China (CityU RFS2021-1S04), and the Shenzhen Municipality Science and Technology Innovation Commission (grant no. SGDXX2020110309300402 [“Modulation and Detection of Terahertz Waves based on Semi-Metallic Two-Dimensional Materials,” CityU]).

AUTHOR CONTRIBUTIONS

Weijun Wang, Y.Z., and Wei Wang contributed equally to this work. J.C.H. and Weijun Wang conceived the project. Y.Z. and Wei Wang performed the DFT calculations and Simcenter STAR CCM+ simulation. Weijun Wang, Y.Z., and Wei Wang conducted AFM, Raman, and XPS characterization and analysis. Weijun Wang, M.L., and Y.M. fabricated the devices and performed the electrical tests and data processing. B.L., Y.Y., D.Y., P.X., D.L., D.C., Q.Q., and S.Y. helped to prepare the samples and

perform the basic material characterizations. W.H., J.C.H., and Weijun Wang wrote the paper. All authors reviewed and commented on the manuscript.

DECLARATION OF INTERESTS

The authors declare no competing interests.

Received: January 3, 2024

Revised: February 23, 2024

Accepted: April 7, 2024

Published: May 7, 2024

REFERENCES

- Aljarb, A., Fu, J.H., Hsu, C.C., Chuu, C.P., Wan, Y., Hakami, M., Naphade, D.R., Yengel, E., Lee, C.J., Brems, S., et al. (2020). Ledge-directed epitaxy of continuously self-aligned single-crystalline nanoribbons of transition metal dichalcogenides. *Nat. Mater.* 19, 1300. <https://doi.org/10.1038/s41563-020-0795-4>.
- Nguyen, V.L., Shin, B.G., Duong, D.L., Kim, S.T., Perello, D., Lim, Y.J., Yuan, Q.H., Ding, F., Jeong, H.Y., Shin, H.S., et al. (2015). Seamless Stitching of Graphene Domains on Polished Copper (111) Foil. *Adv. Mater.* 27, 1376–1382. <https://doi.org/10.1002/adma.201404541>.
- Dean, C.R., Young, A.F., Meric, I., Lee, C., Wang, L., Sorgenfrei, S., Watanabe, K., Taniguchi, T., Kim, P., Shepard, K.L., and Hone, J. (2010). Boron nitride substrates for high-quality graphene electronics. *Nat. Nanotechnol.* 5, 722–726. <https://doi.org/10.1038/nnano.2010.172>.
- Khan, U., Luo, Y., Tang, L., Teng, C., Liu, J., Liu, B., and Cheng, H.M. (2019). Controlled Vapor Solid Deposition of Millimeter-Size Single Crystal 2D Bi₂O₂Se for High-Performance Phototransistors. *Adv. Funct. Mater.* 29, 1807979. <https://doi.org/10.1002/adfm.201807979>.
- Tong, T., Chen, Y., Qin, S., Li, W., Zhang, J., Zhu, C., Zhang, C., Yuan, X., Chen, X., Nie, Z., et al. (2019). Sensitive and Ultrabroadband Phototransistor Based on Two-Dimensional Bi₂O₂Se Nanosheets. *Adv. Funct. Mater.* 29, 1905806. <https://doi.org/10.1002/adfm.201905806>.
- Rhodes, D., Chae, S.H., Ribeiro-Palau, R., and Hone, J. (2019). Disorder in van der Waals heterostructures of 2D materials. *Nat. Mater.* 18, 541–549. <https://doi.org/10.1038/s41563-019-0366-8>.
- Chen, J.H., Jang, C., Xiao, S., Ishigami, M., and Fuhrer, M.S. (2008). Intrinsic and extrinsic performance limits of graphene devices on SiO₂. *Nat. Nanotechnol.* 3, 206–209. <https://doi.org/10.1038/nnano.2008.58>.
- Raja, A., Waldecker, L., Zipfel, J., Cho, Y., Brem, S., Ziegler, J.D., Kulig, M., Taniguchi, T., Watanabe, K., Malic, E., et al. (2019). Dielectric disorder in two-dimensional materials. *Nat. Nanotechnol.* 14, 832–837. <https://doi.org/10.1038/s41565-019-0520-0>.
- Chen, T.A., Chuu, C.P., Tseng, C.C., Wen, C.K., Wong, H.S.P., Pan, S., Li, R., Chao, T.A., Chueh, W.C., Zhang, Y., et al. (2020). Wafer-scale single-crystal hexagonal boron nitride monolayers on Cu (111). *Nature* 579, 219–223. <https://doi.org/10.1038/s41586-020-2009-2>.
- Xu, Y., Liu, T., Liu, K., Zhao, Y., Liu, L., Li, P., Nie, A., Liu, L., Yu, J., Feng, X., et al. (2023). Scalable integration of hybrid high-dielectric materials on two-dimensional semiconductors. *Nat. Mater.* 22, 1078–1084. <https://doi.org/10.1038/s41563-023-01626-w>.
- Chen, J., Liu, Z., Dong, X., Gao, Z., Lin, Y., He, Y., Duan, Y., Cheng, T., Zhou, Z., Fu, H., et al. (2023). Vertically grown ultrathin Bi₂SiO₅ as high-κ single-crystalline gate dielectric. *Nat. Commun.* 14, 4406. <https://doi.org/10.1038/s41467-023-40123-1>.
- An, L., Yu, Y., Cai, Q., Mateti, S., Li, L.H., and Chen, Y.I. (2023). Hexagonal boron nitride nanosheets: Preparation, heat transport property and application as thermally conductive fillers. *Prog. Mater. Sci.* 138, 101154. <https://doi.org/10.1016/j.pmatsci.2023.101154>.
- Liu, K., Jin, B., Han, W., Chen, X., Gong, P., Huang, L., Zhao, Y., Li, L., Yang, S., Hu, X., et al. (2021). A wafer-scale van der Waals dielectric made from an inorganic molecular crystal film. *Nat. Electron.* 4, 906–913. <https://doi.org/10.1038/s41928-021-00683-w>.
- Takenobu, T. (2023). High-κ two-dimensional dielectric. *Nat. Mater.* 22, 811–812. <https://doi.org/10.1038/s41563-023-01567-4>.
- Ji, Q., Zhang, Y., Gao, T., Zhang, Y., Ma, D., Liu, M., Chen, Y., Qiao, X., Tan, P.-H., Kan, M., et al. (2013). Epitaxial monolayer MoS₂ on mica with novel photoluminescence. *Nano Lett.* 13, 3870–3877. <https://doi.org/10.1021/nl401938t>.
- Wu, Z., Tai, G., Liu, R., Hou, C., Shao, W., Liang, X., and Wu, Z. (2021). van der Waals Epitaxial Growth of Borophene on a Mica Substrate toward a High-Performance Photodetector. *ACS Appl. Mater. Inter.* 13, 31808–31815. <https://doi.org/10.1021/acsami.1c03146>.
- Qin, J.-K., Shao, W.-Z., Li, Y., Xu, C.-Y., Ren, D.-D., Song, X.-G., and Zhen, L. (2017). van der Waals epitaxy of large-area continuous ReS₂ films on mica substrate. *RSC Adv.* 7, 24188–24194. <https://doi.org/10.1039/C7RA01748K>.
- Qin, B., Ma, H., Hossain, M., Zhong, M., Xia, Q., Li, B., and Duan, X. (2020). Substrates in the synthesis of two-dimensional materials via chemical vapor deposition. *Chem. Mater.* 32, 10321–10347. <https://doi.org/10.1021/acs.chemmater.0c03549>.
- Wang, N., Pan, X., Wang, P., Wang, Y., He, H., Zeng, Y.-J., Zhang, L., Li, Y., Wang, F., Lu, B., et al. (2022). Is all epitaxy on mica van der Waals epitaxy? *Mater. Today Nano* 20, 100255. <https://doi.org/10.1016/j.mtnano.2022.100255>.
- Zhang, X., He, Y., Li, R., Dong, H., and Hu, W. (2016). 2D Mica Crystal as Electret in Organic Field-Effect Transistors for Multistate Memory. *Adv. Mater.* 28, 3755–3760. <https://doi.org/10.1002/adma.201506356>.
- Weeks, J.R. (1922). The dielectric constant of mica. *Phys. Rev.* 19, 319–322. <https://doi.org/10.1103/PhysRev.19.319>.
- Frisenda, R., Niu, Y., Gant, P., Muñoz, M., and Castellanos-Gomez, A. (2020). Naturally occurring van der Waals materials. *Npj 2d Mater. Appl.* 4, 38. <https://doi.org/10.1038/s41699-020-00172-2>.
- Low, C.G., Zhang, Q., Hao, Y., and Ruoff, R.S. (2014). Graphene Field Effect Transistors with Mica as Gate Dielectric Layers. *Small* 10, 4213–4218. <https://doi.org/10.1002/sml.201303929>.
- Wang, S., Li, Y., Ng, A., Hu, Q., Zhou, Q., Li, X., and Liu, H. (2020). 2D Bi₂Se₃ van der Waals epitaxy on mica for optoelectronics applications. *Nanomater.* 10, 1653. <https://doi.org/10.3390/nano10091653>.
- Khan, U., Luo, Y., Tang, L., Teng, C., Liu, J., Liu, B., and Cheng, H.M. (2019). Controlled vapor-solid deposition of millimeter-size single crystal 2D Bi₂O₂Se for high-performance phototransistors. *Adv. Funct. Mater.* 29, 1807979. <https://doi.org/10.1002/adfm.201807979>.
- Ling, X., Lee, Y.H., Lin, Y., Fang, W., Yu, L., Dresselhaus, M.S., and Kong, J. (2014). Role of the Seeding Promoter in MoS₂ Growth by Chemical Vapor Deposition. *Nano Lett.* 14, 464–472. <https://doi.org/10.1021/nl4033704>.
- van der Zande, A.M., Huang, P.Y., Chenet, D.A., Berkelbach, T.C., You, Y., Lee, G.H., Heinz, T.F., Reichman, D.R., Muller, D.A., and Hone, J.C. (2013). Grains and grain boundaries in highly crystalline monolayer molybdenum disulphide. *Nat. Mater.* 12, 554–561. <https://doi.org/10.1038/nmat3633>.
- Govind Rajan, A., Warner, J.H., Blankschtein, D., and Strano, M.S. (2016). Generalized Mechanistic Model for the Chemical Vapor Deposition of 2D Transition Metal Dichalcogenide Monolayers. *ACS Nano* 10,

- 4330–4344. <https://doi.org/10.1021/acsnano.5b07916>.
29. Wu, J., Tan, C., Tan, Z., Liu, Y., Yin, J., Dang, W., Wang, M., and Peng, H. (2017). Controlled Synthesis of High-Mobility Atomically Thin Bismuth Oxyselenide Crystals. *Nano Lett.* 17, 3021–3026. <https://doi.org/10.1021/acs.nanolett.7b00335>.
30. Hong, C., Tao, Y., Nie, A., Zhang, M., Wang, N., Li, R., Huang, J., Huang, Y., Ren, X., Cheng, Y., and Liu, X. (2020). Inclined Ultrathin Bi₂O₂Se Films: A Building Block for Functional van der Waals Heterostructures. *ACS Nano* 14, 16803–16812. <https://doi.org/10.1021/acsnano.0c05300>.
31. Wang, W., Geng, Y., Qian, Y., Xie, Y., and Liu, X. (1999). Synthesis and characterization of nanocrystalline Bi₂Se₃ by solvothermal method. *Mater. Res. Bull.* 34, 131–134. [https://doi.org/10.1016/S0025-5408\(98\)00203-7](https://doi.org/10.1016/S0025-5408(98)00203-7).
32. Messalea, K.A., Zavabeti, A., Mohiuddin, M., Syed, N., Jannat, A., Atkin, P., Ahmed, T., Walia, S., McConville, C.F., Kalantar-Zadeh, K., et al. (2020). Two-Step Synthesis of Large-Area 2D Bi₂S₃ Nanosheets Featuring High In-Plane Anisotropy. *Adv. Mater. Interfaces* 7, 2001131. <https://doi.org/10.1002/admi.202001131>.
33. Khan, U., Nairan, A., Khan, K., Li, S., Liu, B., and Gao, J. (2023). Salt-Assisted Low-Temperature Growth of 2D Bi₂O₂Se with Controlled Thickness for Electronics. *Small* 19, 2206648. <https://doi.org/10.1002/sml.202206648>.
34. Hossain, M.T., Jena, T., Nath, U., Sarma, M., and Giri, P.K. (2023). Room temperature exciton formation and robust optical properties of CVD-grown ultrathin Bi₂O₂Se crystals on arbitrary substrates. *Nanoscale* 15, 11222–11236. <https://doi.org/10.1039/d3nr01201h>.
35. Yu, J., Han, Y., Zhang, H., Ding, X., Qiao, L., and Hu, J. (2022). Excimer Formation in the Non-Van-Der-Waals 2D Semiconductor Bi₂O₂Se. *Adv. Mater.* 34, 2204227. <https://doi.org/10.1002/adma.202204227>.
36. Chen, Y., Ma, W., Tan, C., Luo, M., Zhou, W., Yao, N., Wang, H., Zhang, L., Xu, T., Tong, T., et al. (2021). Broadband Bi₂O₂Se Photodetectors from Infrared to Terahertz. *Adv. Funct. Mater.* 31, 2009554. <https://doi.org/10.1002/adfm.202009554>.
37. Zhang, J., Peng, Z., Soni, A., Zhao, Y., Xiong, Y., Peng, B., Wang, J., Dresselhaus, M.S., and Xiong, Q. (2011). Raman Spectroscopy of Few-Quintuple Layer Topological Insulator Bi₂Se₃ Nanoplatelets. *Nano Lett.* 11, 2407–2414. <https://doi.org/10.1021/nl200773n>.
38. Han, M., Wu, S., Zhao, X., He, Q., Zhang, B., Xiong, W., Luo, X., and Zheng, Y. (2023). Raman Spectroscopy of the Trapezoidal Bi₂O₂Se. *Adv. Opt. Mater.* 11, 2300344. <https://doi.org/10.1002/adom.202300344>.
39. Poppa, H., and Elliot, A. (1971). The surface composition of mica substrates. *Surf. Sci.* 24, 149–163. [https://doi.org/10.1016/0039-6028\(71\)90225-1](https://doi.org/10.1016/0039-6028(71)90225-1).
40. Huang, L., Yu, Y., Li, C., and Cao, L. (2013). Substrate Mediation in Vapor Deposition Growth of Layered Chalcogenide Nanoplates: A Case Study of SnSe₂. *J. Phys. Chem. C* 117, 6469–6475. <https://doi.org/10.1021/jp400274a>.
41. Sang, X., Li, X., Zhao, W., Dong, J., Rouleau, C.M., Geohegan, D.B., Ding, F., Xiao, K., and Unocic, R.R. (2018). In situ edge engineering in two-dimensional transition metal dichalcogenides. *Nat. Commun.* 9, 2051. <https://doi.org/10.1038/s41467-018-04435-x>.
42. Ren, X., Dong, J., Yang, P., Li, J., Lu, G., Wu, T., Wang, H., Guo, W., Zhang, Z., Ding, F., and Jin, C. (2019). Grain boundaries in chemical-vapor-deposited atomically thin hexagonal boron nitride. *Phys. Rev. Mater.* 3, 014004. <https://doi.org/10.1103/PhysRevMaterials.3.014004>.
43. Dong, J., Zhang, L., Zhang, K., and Ding, F. (2018). How graphene crosses a grain boundary on the catalyst surface during chemical vapour deposition growth. *Nanoscale* 10, 6878–6883. <https://doi.org/10.1039/c7nr06840a>.
44. Zhang, Z., Yang, X., Liu, K., and Wang, R. (2022). Epitaxy of 2D Materials toward Single Crystals. *Adv. Sci.* 9, 2105201. <https://doi.org/10.1002/advs.202105201>.
45. Ji, Q., Kan, M., Zhang, Y., Guo, Y., Ma, D., Shi, J., Sun, Q., Chen, Q., Zhang, Y., and Liu, Z. (2015). Unravelling Orientation Distribution and Merging Behavior of Mono layer MoS₂ Domains on Sapphire. *Nano Lett.* 15, 198–205. <https://doi.org/10.1021/nl503373x>.
46. Humphreys, J.F. (1996). *A Course in Group Theory (USA: Oxford University Press)*.
47. Dong, J., Zhang, L., Dai, X., and Ding, F. (2020). The epitaxy of 2D materials growth. *Nat. Commun.* 11, 5862. <https://doi.org/10.1038/s41467-020-19752-3>.
48. Kim, T.S., Noh, G., Kwon, S., Kim, J.Y., Dhakal, K.P., Oh, S., Chai, H.J., Park, E., Kim, I.S., Lee, E., et al. (2024). Diffusion Control on the Van der Waals Surface of Monolayers for Uniform Bi-Layer MoS₂ Growth. *Adv. Funct. Mater.* 2312365. <https://doi.org/10.1002/adfm.202312365>.
49. Sebastian, A., Pendurthi, R., Choudhury, T.H., Redwing, J.M., and Das, S. (2021). Benchmarking monolayer MoS₂ and WS₂ field-effect transistors. *Nat. Commun.* 12, 693. <https://doi.org/10.1038/s41467-020-20732-w>.
50. Chang, Y.H., Zhang, W., Zhu, Y., Han, Y., Pu, J., Chang, J.K., Hsu, W.T., Huang, J.K., Hsu, C.L., Chiu, M.H., et al. (2014). Monolayer MoSe₂ Grown by Chemical Vapor Deposition for Fast Photodetection. *ACS Nano* 8, 8582–8590. <https://doi.org/10.1021/nn503287m>.
51. Uchiyama, Y., Kutana, A., Watanabe, K., Taniguchi, T., Kojima, K., Endo, T., Miyata, Y., Shinohara, H., and Kitaura, R. (2019). Momentum-forbidden dark excitons in hBN-encapsulated monolayer MoS₂. *Npj 2d Mater. Appl.* 3, 26. <https://doi.org/10.1038/s41699-019-0108-4>.
52. Xu, L., Zhang, P., Jiang, H., Wang, X., Chen, F., Hu, Z., Gong, Y., Shang, L., Zhang, J., Jiang, K., and Chu, J. (2019). Large-Scale Growth and Field-Effect Transistors Electrical Engineering of Atomic-Layer SnS₂. *Small* 15, 1904116. <https://doi.org/10.1002/sml.201904116>.
53. Shafi, A.M., Uddin, M.G., Cui, X., Ali, F., Ahmed, F., Radwan, M., Das, S., Mehmood, N., Sun, Z., and Lipsanen, H. (2023). Strain Engineering for Enhancing Carrier Mobility in MoTe₂ Field-Effect Transistors. *Adv. Sci.* 10, 2303437. <https://doi.org/10.1002/advs.202303437>.
54. Li, L., Wang, W., Chai, Y., Li, H., Tian, M., and Zhai, T. (2017). Few-Layered PtS₂ Phototransistor on h-BN with High Gain. *Adv. Funct. Mater.* 27, 1701011. <https://doi.org/10.1002/adfm.201701011>.
55. Liu, H., Chen, L., Zhu, H., Sun, Q.Q., Ding, S.J., Zhou, P., and Zhang, D.W. (2020). Atomic layer deposited 2D MoS₂ atomic crystals: from material to circuit. *Nano Res.* 13, 1644–1650. <https://doi.org/10.1007/s12274-020-2787-8>.
56. Zhou, N., Gan, L., Yang, R., Wang, F., Li, L., Chen, Y., Li, D., and Zhai, T. (2019). Nonlayered two-dimensional defective semiconductor γ-Ga₂S₃ toward broadband photodetection. *ACS Nano* 13, 6297–6307. <https://doi.org/10.1021/acsnano.9b00276>.
57. Wu, J., Yuan, H., Meng, M., Chen, C., Sun, Y., Chen, Z., Dang, W., Tan, C., Liu, Y., Yin, J., et al. (2017). High electron mobility and quantum oscillations in non-encapsulated ultrathin semiconducting Bi₂O₂Se. *Nat. Nanotechnol.* 12, 530–534. <https://doi.org/10.1038/nnano.2017.43>.
58. Pudasaini, P.R., Oyedele, A., Zhang, C., Stanford, M.G., Cross, N., Wong, A.T., Hoffman, A.N., Xiao, K., Duscher, G., Mandrus, D.G., et al. (2018). High-performance multilayer WSe₂ field-effect transistors with carrier type control. *Nano Res.* 11, 722–730. <https://doi.org/10.1007/s12274-017-1681-5>.
59. Zhou, N., Zhang, Z., Wang, F., Li, J., Xu, X., Li, H., Ding, S., Liu, J., Li, X., Xie, Y., et al. (2022). Spin Ordering Induced Broadband Photodetection Based on Two-Dimensional Magnetic Semiconductor α-MnSe. *Adv. Sci.* 9, 2202177. <https://doi.org/10.1002/advs.202202177>.
60. Wang, Z., Wang, P., Wang, F., Ye, J., He, T., Wu, F., Peng, M., Wu, P., Chen, Y., Zhong, F., et al. (2020). A Noble Metal Dichalcogenide for High-Performance Field-Effect Transistors and Broadband Photodetectors. *Adv. Funct. Mater.* 30, 1907945. <https://doi.org/10.1002/adfm.201907945>.
61. Ai, W., Chen, J., Dong, X., Gao, Z., He, Y., Liu, Z., Fu, H., Luo, F., and Wu, J. (2022). High Mobility and Quantum Oscillations in Semiconducting Bi₂O₂Te Nanosheets Grown by Chemical Vapor Deposition. *Nano Lett.* 22, 7659–7666. <https://doi.org/10.1021/acs.nanolett.2c02891>.
62. Fu, Q., Zhu, C., Zhao, X., Wang, X., Chaturvedi, A., Zhu, C., Wang, X., Zeng, Q., Zhou, J., Liu, F., et al. (2019). Ultrasensitive 2D Bi₂O₂Se phototransistors on silicon substrates. *Adv. Mater.* 31, 1804945. <https://doi.org/10.1002/adma.201804945>.
63. Tan, C., Tang, M., Wu, J., Liu, Y., Li, T., Liang, Y., Deng, B., Tan, Z., Tu, T., Zhang, Y., et al. (2019). Wafer-Scale Growth of Single-Crystal 2D Semiconductor on Perovskite Oxides for High-Performance Transistors. *Nano Lett.* 19, 2148–2153. <https://doi.org/10.1021/acsnano.9b00381>.
64. Wu, Z., Jiang, Z., Song, P., Tian, P., Hu, L., Liu, R., Fang, Z., Kang, J., and Zhang, T.Y. (2019).

- Nanowire-Seeded Growth of Single-Crystalline (010) β - Ga_2O_3 Nanosheets with High Field-Effect Electron Mobility and On/Off Current Ratio. *Small* 15, 1900580. <https://doi.org/10.1002/sml.201900580>.
65. Wang, L., Wang, X., Zhang, Y., Li, R., Ma, T., Leng, K., Chen, Z., Abdelwahab, I., and Loh, K.P. (2020). Exploring ferroelectric switching in α - In_2Se_3 for neuromorphic computing. *Adv. Funct. Mater.* 30, 2004609. <https://doi.org/10.1002/adfm.202004609>.
66. Jiang, B., Zou, X., Su, J., Liang, J., Wang, J., Liu, H., Feng, L., Jiang, C., Wang, F., He, J., and Liao, L. (2018). Impact of Thickness on Contact Issues for Pinning Effect in Black Phosphorus Field-Effect Transistors. *Adv. Funct. Mater.* 28, 1801398. <https://doi.org/10.1002/adfm.201801398>.
67. Wells, S.A., Henning, A., Gish, J.T., Sangwan, V.K., Lauhon, L.J., and Hersam, M.C. (2018). Suppressing Ambient Degradation of Exfoliated InSe Nanosheet Devices via Seeded Atomic Layer Deposition Encapsulation. *Nano Lett.* 18, 7876–7882. <https://doi.org/10.1021/acs.nanolett.8b03689>.
68. Chubarov, M., Choudhury, T.H., Hickey, D.R., Bachu, S., Zhang, T., Sebastian, A., Bansal, A., Zhu, H., Trainor, N., Das, S., et al. (2021). Wafer-Scale Epitaxial Growth of Unidirectional WS_2 Monolayers on Sapphire. *ACS Nano* 15, 2532–2541. <https://doi.org/10.1021/acsnano.0c06750>.
69. Zhang, C., Wu, J., Sun, Y., Tan, C., Li, T., Tu, T., Zhang, Y., Liang, Y., Zhou, X., Gao, P., and Peng, H. (2020). High-Mobility Flexible Oxyselenide Thin-Film Transistors Prepared by a Solution-Assisted Method. *J. Am. Chem. Soc.* 142, 2726–2731. <https://doi.org/10.1021/jacs.9b11668>.
70. Li, T., Tu, T., Sun, Y., Fu, H., Yu, J., Xing, L., Wang, Z., Wang, H., Jia, R., Wu, J., et al. (2020). A native oxide high- κ gate dielectric for two-dimensional electronics. *Nat. Electron.* 3, 473–478. <https://doi.org/10.1038/s41928-020-0444-6>.
71. Wang, W., Meng, Y., Wang, W., Zhang, Z., Xie, P., Lai, Z., Bu, X., Li, Y., Liu, C., Yang, Z., et al. (2022). Highly Efficient Full van der Waals 1D p-Te/2D n- $\text{Bi}_2\text{O}_2\text{Se}$ Heterodiodes with Nanoscale Ultra-Photosensitive Channels. *Adv. Funct. Mater.* 32, 2203003. <https://doi.org/10.1002/adfm.202203003>.
72. Wang, W., Meng, Y., Zhang, Y., Zhang, Z., Wang, W., Lai, Z., Xie, P., Li, D., Chen, D., Quan, Q., et al. (2023). Electrically Switchable Polarization in $\text{Bi}_2\text{O}_2\text{Se}$ Ferroelectric Semiconductors. *Adv. Mater.* 35, 2210854. <https://doi.org/10.1002/adma.202210854>.
73. Kresse, G., and Furthmüller, J. (1996). Efficient iterative schemes for ab initio total-energy calculations using a plane-wave basis set. *Phys. Rev. B* 54, 11169–11186. <https://doi.org/10.1103/PhysRevB.54.11169>.
74. Blöchl, P. (1994). Projector augmented-wave method. *Phys. Rev. B* 50, 17953–17979. <https://doi.org/10.1103/PhysRevB.50.17953>.
75. Perdew, J.P., Burke, K., and Ernzerhof, M. (1996). Generalized Gradient Approximation Made Simple. *Phys. Rev. Lett.* 77, 3865–3868. <https://doi.org/10.1103/PhysRevLett.77.3865>.
76. Grimme, S., Antony, J., Ehrlich, S., and Krieg, H. (2010). A consistent and accurate ab initio parametrization of density functional dispersion correction (DFT-D) for the 94 elements H-Pu. *J. Chem. Phys.* 132, 154104. <https://doi.org/10.1063/1.3382344>.

Matter, Volume 7

Supplemental information

Orientation-engineered 2D electronics

on van der Waals dielectrics

Weijun Wang, Yuxuan Zhang, Wei Wang, Min Luo, You Meng, Bowen Li, Yan Yan, Di Yin, Pengshan Xie, Dengji Li, Dong Chen, Quan Quan, SenPo Yip, Weida Hu, and Johnny C. Ho

Supplemental Notes

Note S1. Growth dynamics on the mica substrate.

At high growth temperatures above 620 °C, a thermodynamics-controlled synthesis situation is more favorable due to the higher migration rate of adatoms. A structure terminated by (00n) planes with the fewest dangling bonds is the most stable state for 2D layered materials.¹ Conversely, as the weight ratio of precursors and growth temperature varies, the relative concentrations of the reactants in the growth vapor change. This could affect the initial nucleation rate and crystal growth, forming an intermediate state of the kinetics-dominated and thermodynamics-controlled synthesis of in-plane/inclined Bi₂O₂Se.² The inclined growth of 2D Bi₂O₂Se nanoflakes can be attributed to a reduced substrate temperature, which decreases the kinetic energy of the precursor adatoms, suppressing their diffusion on mica and activating the inclined growth of 2D Bi₂O₂Se.³ The epitaxy of Bi₂Se₃ will be gradually dominant as the Bi₂Se₃/Bi₂O₃ weight ratio increases, attributed to the reduction effect of excess Se vapor decomposed by Bi₂Se₃.⁴

Note S2. Reasons for the redshift of inclined and in-plane Bi₂O₂Se A1g peak

Their dominant reasons are quite different. For the inclined Bi₂O₂Se, a significantly temperature-dependent volume expansion and inharmonic phonon–phonon coupling within the crystal can be expected, as a stronger light absorption in inclined Bi₂O₂Se may heat the samples. Compared with the flatwise stress-free Bi₂O₂Se on mica, the as-grown in-plane Bi₂O₂Se is merely subjected to strains imposed upon it by the host mica substrate after high-temperature CVD growth.⁵

Note S3. Derivation of the number of equivalent but different Directions

Here, G_{Mica} , G_{2D} , and $G_{2D@Mica}$ are symmetry groups of the substrate, the 2D material, and the 2D material–substrate system. $|G_{\text{Mica}}|$ and $|G_{2D@Mica}|$ are the orders of G_{Mica} and $G_{2D@Mica}$, and $N_1 = |G_{\text{Mica}}|/|G_{2D@Mica}|$ is the number of equivalent but different directions (N_E) of the 2D material on the substrate.

$$N_E = \frac{|G_{\text{sub}}|}{|G_{2D@sub}|}$$

which is derived from the Lagrange's theorem of the group theory.

The symmetry group of the system of a 2D material on a mica substrate, $G_{2D@Mica}$, must be a subgroup of the symmetric group of the substrate, G_{Mica} , because any symmetric operation of $G_{2D@Mica}$ will not change the substrate. From Lagrange's theorem, we have the following relationship between the order of G_{Mica} (the number of nonequivalent symmetry operations of G_{Mica}) and that of its subgroup, $G_{2D@Mica}$:

$$|G_{\text{Mica}}| = [G_{\text{Mica}} : G_{2D@Mica}] |G_{2D@Mica}|$$

where $|G_{\text{Mica}}|$ and $|G_{2D@Mica}|$ are the orders of G_{Mica} and $G_{2D@Mica}$, respectively. $N = [G_{\text{Mica}} : G_{2D@Mica}]$ is the number of nonequivalent left cosets of $G_{2D@Mica}$ in G_{Mica} . According to the Lagrange's theorem, G_{Sub} can be constructed as:

$$G_{\text{Mica}} = g_1 G_{2D@Mica} \cup g_2 G_{2D@Mica} \cup \dots \cup g_i G_{2D@Mica} \cup \dots \cup g_N G_{2D@Mica}$$

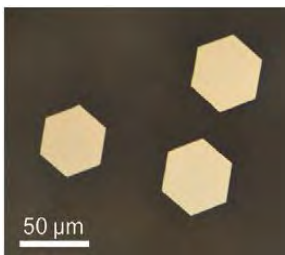
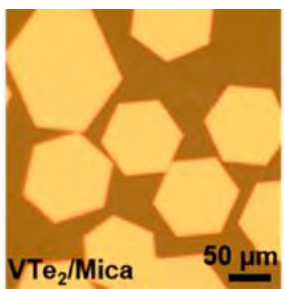
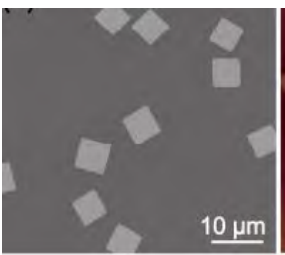
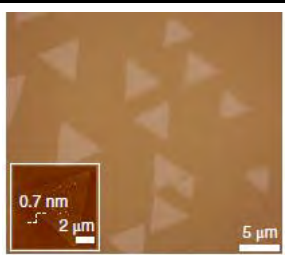
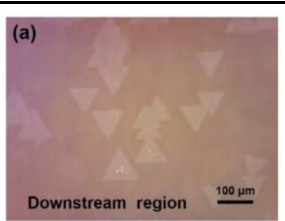
Where $g_i \in G_{\text{Mica}}$, $g_1 = E$, and $g_i G_{2D@Mica} \neq g_j G_{2D@Mica}$ unless $i = j$. Except for $g_1 G_{2D@Mica} = G_{2D@Mica}$, applying all symmetric operations of a left coset, $g_i G_{2D@Mica}$, to the system of 2D@Mica will change the alignment of the 2D material to an equivalent but different direction. So, the number of equivalent but different directions of a 2D material on a substrate is the number of nonequivalent left cosets of $G_{2D@Mica}$ in G_{Mica} :

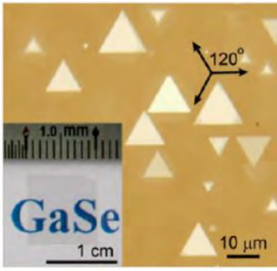


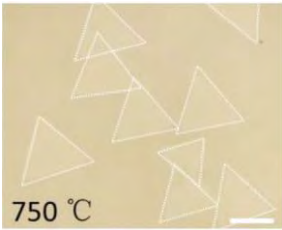

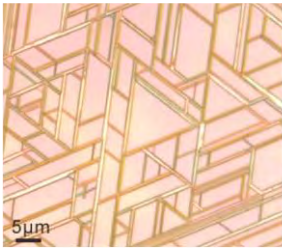
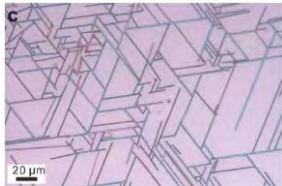
$$N = [G_{\text{Mica}} : G_{2D@Mica}] = |G_{\text{Mica}}|/|G_{2D@Mica}|$$

where $|G_{\text{Mica}}|$ and $|G_{2\text{D@Mica}}|$ are the orders, or numbers of different symmetry operations, of G_{Mica} and $G_{2\text{D@Mica}}$, respectively.

Supplemental Tables

Table S1. Summary of the number of equivalents of 2D materials. The number of equivalent but different orientations of 2D materials is based on the interplay between their symmetries and mica substrates.

2D Materials (Ref.)	Experimental Observation			Theoretical Prediction	
	Crystal Structure 2D Materials Alignment	N	θ	N	θ
h-FeTe ₂ ^{6,7}		1	0°	1	0°
1T-VTe ₂ ⁸		1	0°	1	0°
SnSe ^{9,10}		3	0°, 30° and 60°	3	0°, 30° and 60°
2H MoS ₂ ¹¹		2	0° and 60°	2	0° and 60°
WSe ₂ ¹²		2	0° and 60°	2	0° and 60°

GaSe ¹³		2	0° and 60°	2	0° and 60°
InSe ¹⁴		2	0° and 60°	2	0° and 60°
α-MnSe ¹⁵		2	0° and 60°	2	0° and 60°
trigonal Cr ₂ S ₃ ¹⁶		2	0° and 60°	2	0° and 60°
2H-PbI ₂ ¹⁷		2	0° and 60°	2	0° and 60°
CsPbBr ₃ ¹⁸		3	0°, 30° and 60°	3	0°, 30° and 60°
CsSnI ₃ ¹⁹		3	0°, 30° and 60°	3	0°, 30° and 60°

N represents the number of alignments, and θ represents the misorientation angle of 2D grains, respectively. Reproduced with permission for the above figures, accordingly.

Table S2. Performance comparison with typical 2D materials reported thus far.

Material	Thickness (nm)	Method	Dielectric	$ V_{GS} _{max}$ (V)	V_{DS} (V)	On/off ratio	Mobility ($cm^2 V^{-1} s^{-1}$)
PtS ₂ ²⁰	6.2	ME	Al ₂ O ₃	12	0.5	1.55×10^6	62
MoS ₂ ²¹	0.35	CVD	SiO ₂ /Si	100	1	1.2×10^7	5
α -In ₂ Se ₃ ²²	20-50	ME	Al ₂ O ₃	10	0.1	$\sim 10^5$	30-90
BP ²³	7	ME	SiO ₂	60	1	10^5	-
InSe ²⁴	6	ALD	SiO ₂	60	2	8×10^5	-
β -Ga ₂ O ₃ ²⁵	10	CVD	SiO ₂	50	5	10^7	38
Bi ₂ O ₂ Te ²⁶	7.9	CVD	Al ₂ O ₃	8	0.2	10^3	500
WS ₂ ²⁷	-	CVD	Al ₂ O ₃	15	0.2	10^7	16
Bi ₂ O ₂ Se ^{3,28-32}	8	CVD	SiO ₂	50	0.5	10^7	107
	~ 8.5	SA	HfO ₂	7	0.1	10^5	74
	~ 10	CVD	HfO ₂	3	2	10^5	150
	-	CVD	Bi ₂ SeO ₅	1.5	0.5	10^5	250
	9.3	CVD	SiO ₂	60	1	10^4	230
	10.5	CVD	HfO ₂	8	0.1	10^4	450
	3.2				-	10^6	20
This Work (Bi ₂ O ₂ Se)	3.4 (≈ 6 layers)	CVD	Mica/SiO₂	15	0.06	1.4×10^7	22.3\pm1.2

ME, mechanical exfoliation; CVD, chemical vapor deposition; ALD, atomic layer deposition; SA, solution-assisted method.

Supplemental Figures

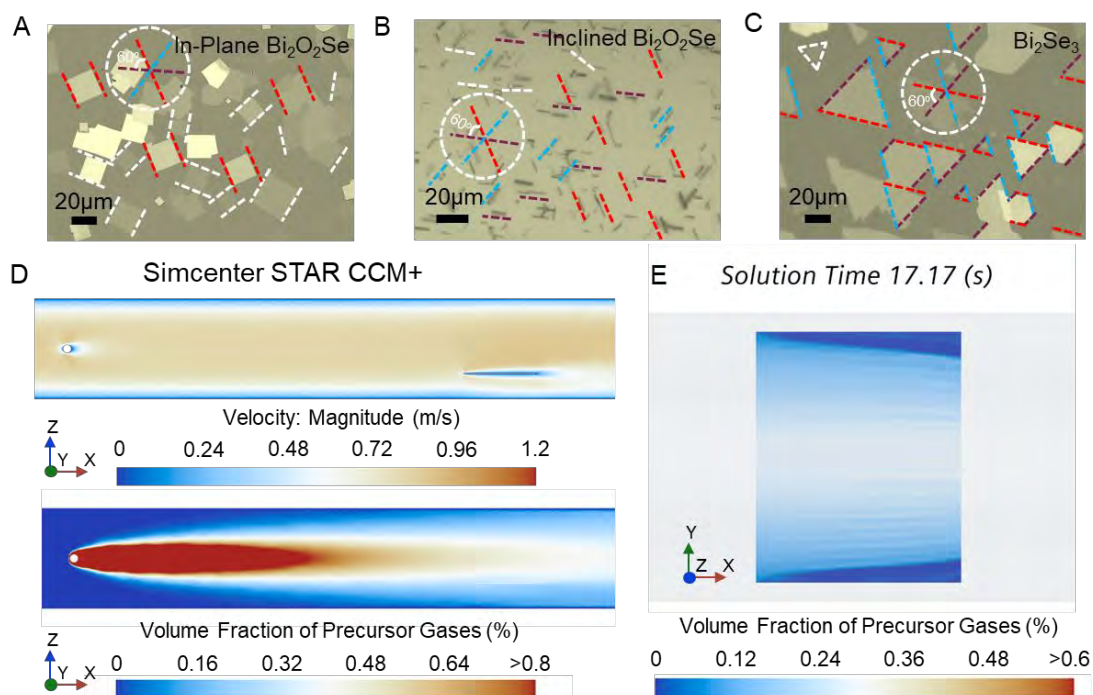


Figure S1. Experimental and simulation results of conventional CVD strategy. (A-C) Typical OM images of the gradient distribution of products, including in-plane $\text{Bi}_2\text{O}_2\text{Se}$, inclined $\text{Bi}_2\text{O}_2\text{Se}$, and Bi_2Se_3 , respectively. The relative misorientation growth of those 2D material flakes is painted in white. (D) Simulated distribution of carrier gas velocity (upper) and precursor concentration field (lower) using Simcenter STAR CCM+ software for conventional CVD system based on the experimental parameters. (E) Simulated precursor concentration ($\sim 2.4\%$) on the top surface of the mica substrate at equilibrium with a solution time of 17.17 s.

As shown in Figure S1A-C, disordered epitaxial growth on mica, which is related to the mass transport process of the precursors, is observed for each product. Thus, the commercial software Simcenter STAR-CCM+, a powerful solution for solving multidisciplinary problems in both fluid and solid mechanics, is utilized to simulate the precursor mass transport in our CVD system. Note that considering the proximity of the Bi_2O_3 and Bi_2Se_3 , a point source with continuous mass flow was considered to simplify the mass transport process. Figure 1G (upper) demonstrates the simulated velocity distribution under laminar flow in the conventional CVD system.³³ The precursor mixture exhibits a rapid concentration dissipation before approaching destined growth substrates (Figure 1G (lower)), resulting in the poor controllability of the product.^{34,35} Figure 1H shows the simulated precursor concentration ($\sim 2.4\%$) on the top surface of the mica substrate at equilibrium, demonstrating a sharp concentration gradient of precursor on the growth substrate concerning source concentration ($c_0=100\%$), thus making CVD growth challenging to control.^{36,37} For example, the ultralow precursor concentration on the growth substrate would lead to the formation of dendritic morphologies in 2D TMDCs synthesis.³⁴

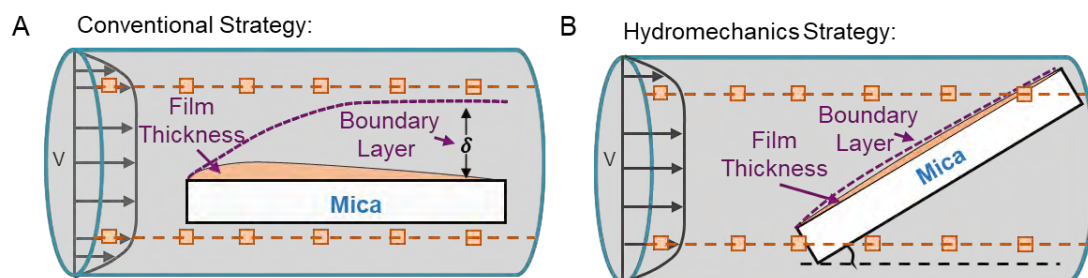


Figure S2. Comparison between conventional and hydromechanics strategy. (A) Schematic control of deposition uniformity in a conventional CVD system, where the substrate is parallel to gas flow. In the conventional deposition system, the gas flow is essentially constant, and the boundary layer gradually increases in thickness downstream. In contrast, the thickness of the deposit will decrease as the distance from the tube inlet increases. (B) Control of deposition uniformity using the hydromechanics strategy with a tilted substrate. It is evident that it is feasible to manage both reaction and deposition effectively with appropriate manipulation of process parameters and reactor geometry.³⁸ The thickness decrease can be offset with a more constant thickness obtained simply by tilting the substrate. This increases the gas velocity due to the flow constriction; the Reynolds number increases, the boundary layer decreases, and the deposition rate becomes more uniform.

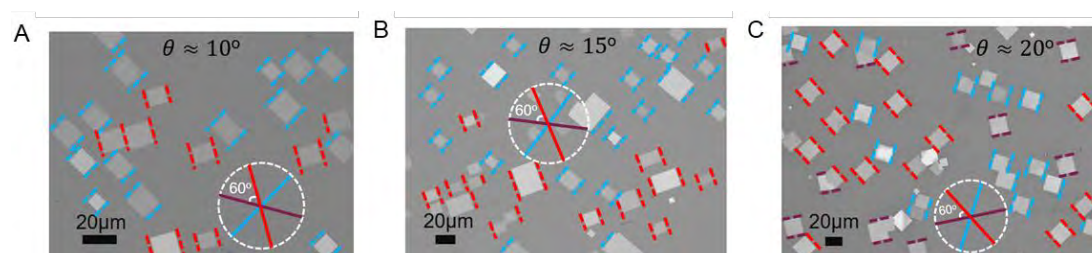


Figure S3. Controllability of hydromechanics CVD strategy. (A-C) OM of the as-grown in-plane $\text{Bi}_2\text{O}_2\text{Se}$ flakes. The number of equivalent but distinct alignments of the in-plane $\text{Bi}_2\text{O}_2\text{Se}$ on mica substrate will change from 2 to 3 directions, which is consistent with our DFT calculations since two of the three angles between the Bi_2Se_3 edge direction and the closely packed direction of K^+ have the same binding energy. This also demonstrates the excellent controllability of the CVD system, where the inclined mica substrate can serve as a "valve" to regulate the flow velocity and precursor concentration field via changing the inclined angle of the growth substrate owing to the limited tube size (1 inch). By simply adjusting the tilted angle of the growth substrate, it becomes possible to manage the distribution and concentration of the vapor precursor across the substrate more precisely. Leveraging better control over the concentration and distribution of the vapor precursor, the hydrodynamic CVD system offers a more refined approach to depositing 2D materials with the desired orientation that is more energy-favorable.

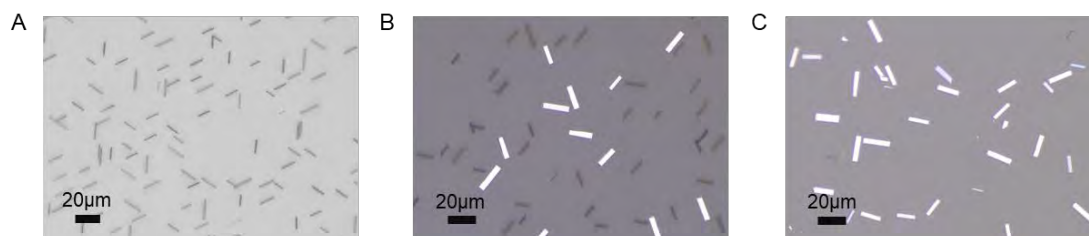


Figure S4. Inclined growth of $\text{Bi}_2\text{O}_2\text{Se}$ flakes. (A) OM of the as-grown inclined $\text{Bi}_2\text{O}_2\text{Se}$ flakes. (B) OM of the inclined $\text{Bi}_2\text{O}_2\text{Se}$ flakes after moderate sonication in DI water for 1 s. Only partially inclined $\text{Bi}_2\text{O}_2\text{Se}$ flakes, referred to as flatwise $\text{Bi}_2\text{O}_2\text{Se}$ flakes, fall down, keeping good orientations on the mica substrate. (C) Inclined $\text{Bi}_2\text{O}_2\text{Se}$ flakes completely convert into flatwise $\text{Bi}_2\text{O}_2\text{Se}$ as the sonication time increases to 5 s.

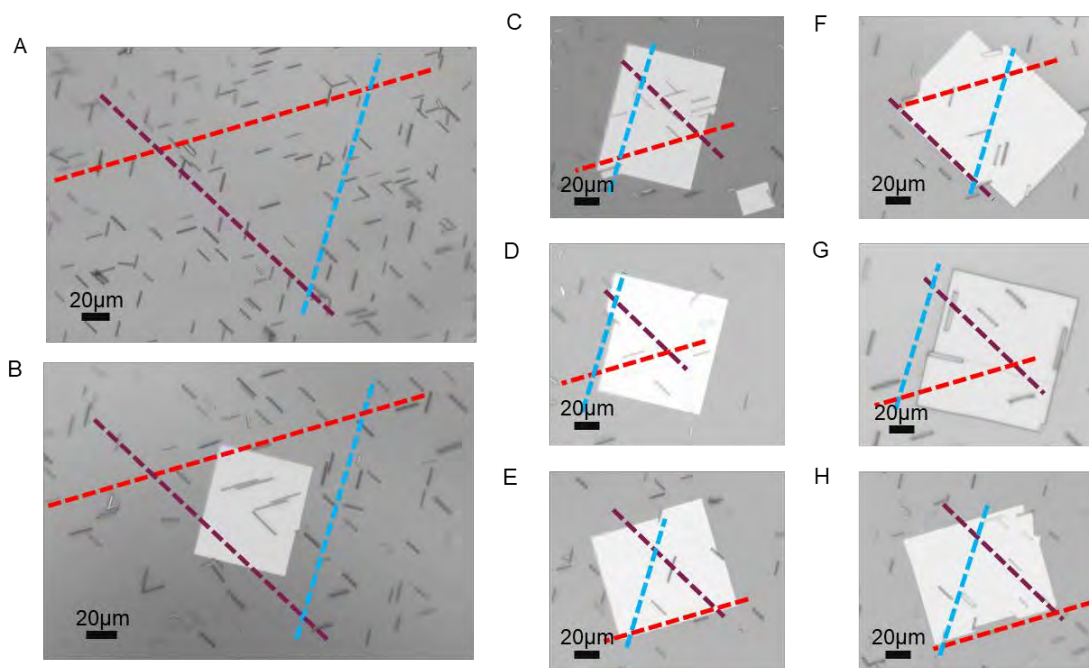


Figure S5. orientations and morphology evolution. (A-H) OM of the as-grown inclined and in-plane $\text{Bi}_2\text{O}_2\text{Se}$ flakes if the heating temperature in the furnace center is above 620°C and the tilted angle of mica substrate is around 20° with a weight ratio of $\text{Bi}_2\text{Se}_3/\text{Bi}_2\text{O}_3$ above 0.2. As shown in these figures, the inclined growth of $\text{Bi}_2\text{O}_2\text{Se}$ is relatively dominant compared with the in-plane $\text{Bi}_2\text{O}_2\text{Se}$. This can be attributed to the low melting points and decomposition temperature of Bi_2Se_3 , which produces an oxygen-deficient environment, improving the inclined growth of $\text{Bi}_2\text{O}_2\text{Se}$ accordingly.^{3,39}

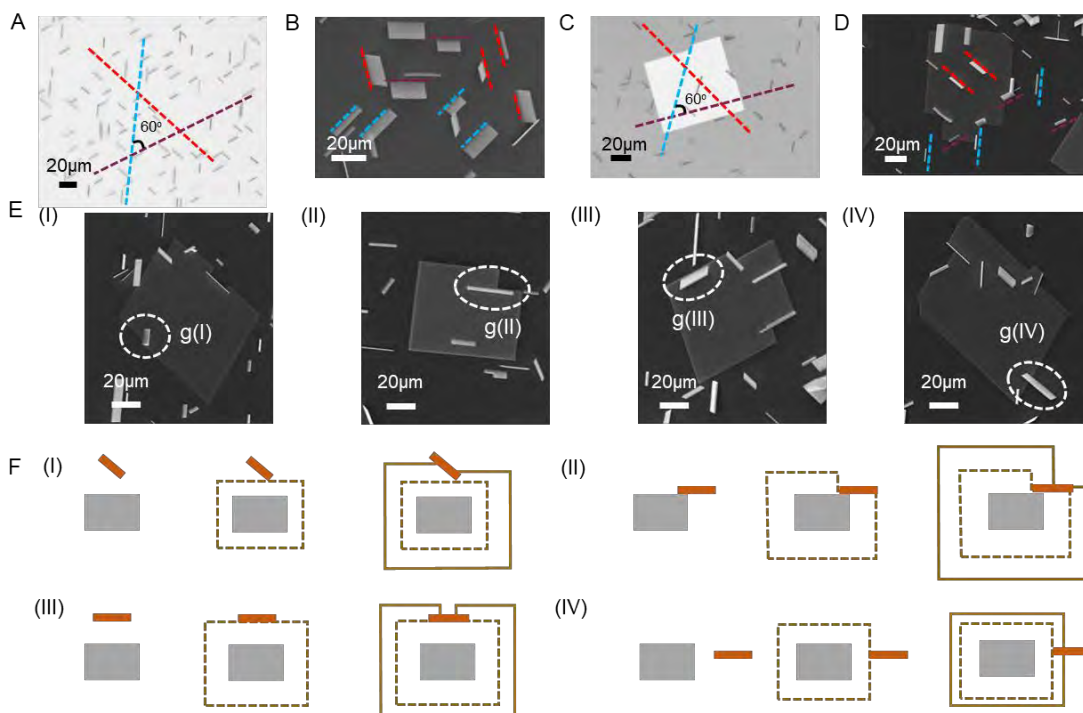


Figure S6. Models of typical merging scenarios. (A-B) OM and corresponding SEM of the inclined $\text{Bi}_2\text{O}_2\text{Se}$ with 3 equivalent but distinct alignments on the mica substrate, respectively. (C-D) OM and related SEM image of the mixed growth of inclined/ in-plane $\text{Bi}_2\text{O}_2\text{Se}$ flakes on mica substrate. (E) Typical SEM images of the mixed inclined/ in-plane $\text{Bi}_2\text{O}_2\text{Se}$ flakes reveal the coupling epitaxial relationships between inclined and in-plane growth of $\text{Bi}_2\text{O}_2\text{Se}$ flakes. The growth of the 2D materials in a CVD system is synergistically controlled by the feeding rate of the precursor from the vapor environment and the precursor from the substrate absorption. The

growth of inclined $\text{Bi}_2\text{O}_2\text{Se}$ has a significant impact on the diffusion of precursors on the substrate, which in turn influences the growth behavior of in-plane $\text{Bi}_2\text{O}_2\text{Se}$. This relationship highlights the intricate dynamics between the orientation of deposited layers and their effect on subsequent material deposition processes. (F) Schematic dynamic models for the merging processes of inclined and in-plane $\text{Bi}_2\text{O}_2\text{Se}$. The solid lines demonstrate the actual boundaries when an in-plane $\text{Bi}_2\text{O}_2\text{Se}$ flake is merged with the inclined $\text{Bi}_2\text{O}_2\text{Se}$ flakes, whereas the dotted lines demonstrate the possible intermediate merging states according to the crystal growth rule of the Bravais.⁴⁰ The schematic dynamic models delineate the merging processes of inclined and in-plane $\text{Bi}_2\text{O}_2\text{Se}$, corresponding to four typical merging scenarios as illustrated in Figure S6E. These models provide a visual representation and theoretical framework for understanding how inclined and in-plane $\text{Bi}_2\text{O}_2\text{Se}$ structures coalesce during the growth process, highlighting the underlying mechanisms and potential outcomes of each scenario. The models are designed to capture the complexity of the interactions between different morphologies of $\text{Bi}_2\text{O}_2\text{Se}$ as they merge together, offering insights into the formation mechanism of distinct final morphologies.

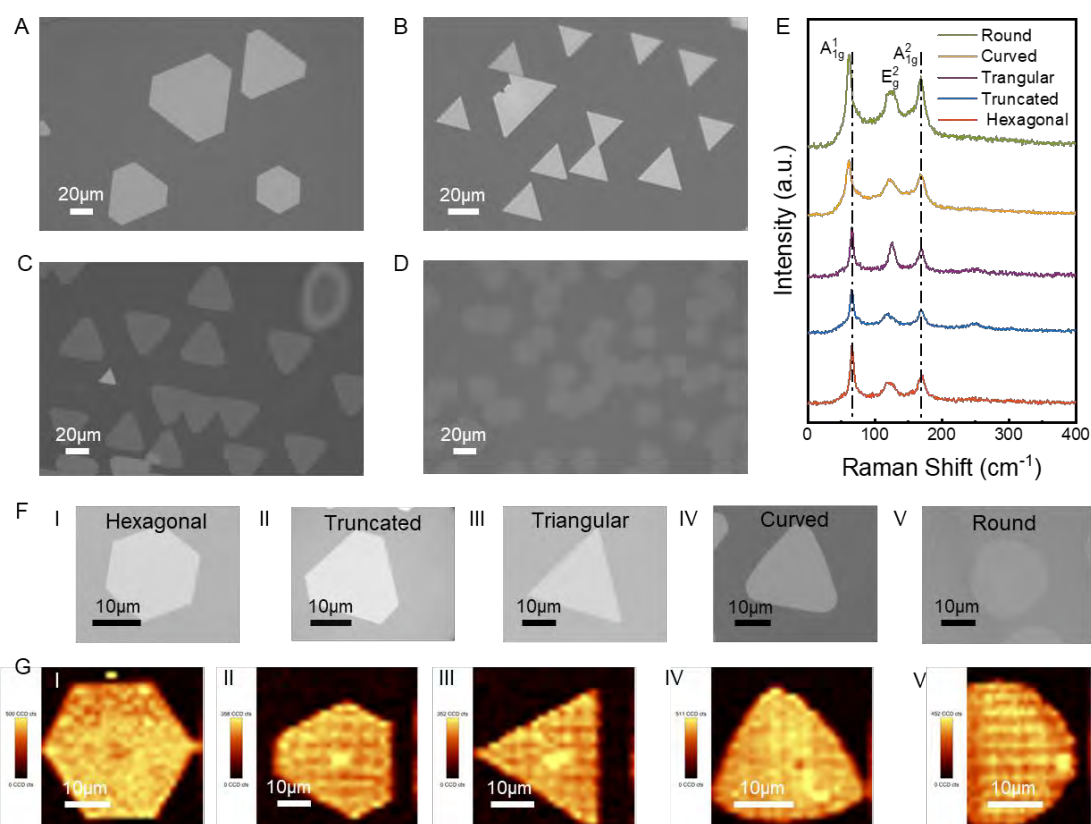


Figure S7. Morphologies of as-grown Bi_2Se_3 flakes. (A-D) OM images of as-grown Bi_2Se_3 products with distinct morphologies on the mica substrate. (E) Raman spectra of the Bi_2Se_3 flakes with hexagonal, truncated, triangular, curved, and round crystal shapes. As demonstrated in the Raman spectra, no obvious Raman peak shifts are observed in different-shaped Bi_2Se_3 . (F) Separated OM image of the distinctly shaped Bi_2Se_3 flake, marked by the number of I-V, respectively. (G) Related Raman mapping of the Bi_2Se_3 A_{1g} peak, corresponding to the distinctly shaped Bi_2Se_3 flakes, respectively.

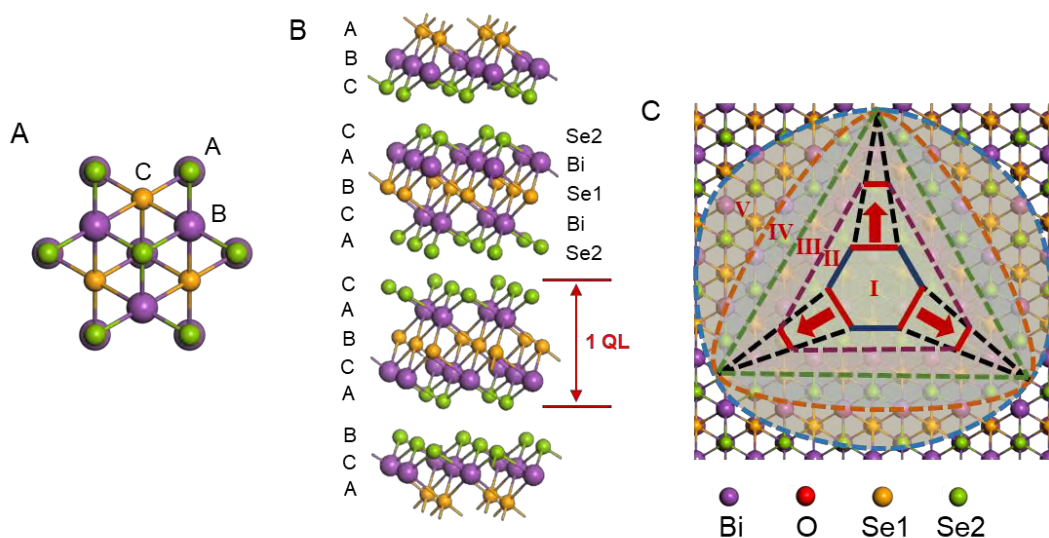


Figure S8. Atomic models of morphology evolutions of Bi₂Se₃ flakes. (A) Atomic structure of a Bi₂Se₃ flake within one quintuple layer from the top view, which has three distinct positions, referring to A, B, and C. (B) Side view of the quintuple layer Bi₂Se₃ structure. Each quintuple layer (1 QL ≈ 9.55 Å) has five atomic layers Se2-Bi-Se1-Bi-Se2, and interlayer QLs are weakly bonded by van der Waals force while in each QL is bonded by strong covalent bonding. (C) Atomic illustration of the relations between domain shapes and Bi₂Se₃ crystal structure. The formation mechanism of different domain shapes will be explained in detail in Figure S9.

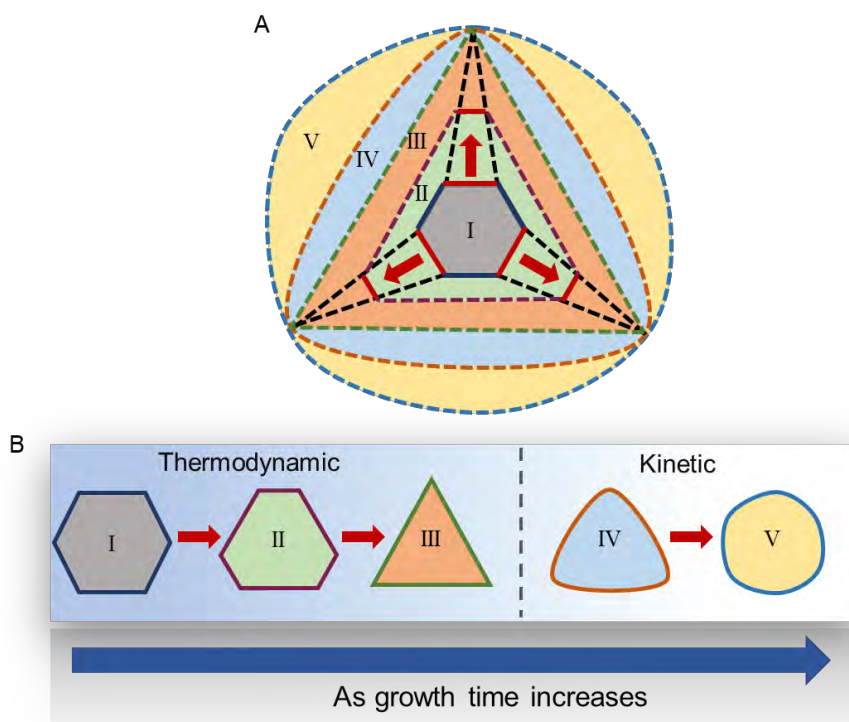


Figure S9. Relations between morphologies and growth dynamics. (A) Schematic illustration of the Bi₂Se₃ morphologies' evolution is marked by I, II, III, IV, and V, respectively. (B) Illustration of the relations between domain shapes and growth dynamics as the growth time increases.

The formation of various domain shapes, such as hexagonal, truncated, triangular, curved, and round shapes, is governed by the interplay between the thermodynamic and kinetic growth dynamics. According to the crystal growth rule of the Bravais⁴⁰, ideal crystals are stable with facets with the lowest growth speed in their normal directions, while those with the highest growth speed in their normal directions disappear. This conclusion is consistent with the results

of the Bi_2Se_3 morphology evolution observed from Stage I to Stage III. During the thermodynamic growth mode, the dominant domain shapes observed are equilateral triangles (Stage I), which emerge when the precursor rate is moderate. However, the growth mode rapidly transitions to kinetic control for Bi_2Se_3 when there is an excessive supply of precursor. In this scenario, the surplus precursor vapor induces a shift from anisotropic growth to isotropic growth, simultaneously promoting high growth rates in all directions. Consequently, Bi_2Se_3 flakes with positive (Stage IV) and even round edges (Stage V) are formed as a result of this isotropic growth phenomenon.⁴¹ The underlying thermodynamic and kinetic processes, as well as the availability of precursor, thus play crucial roles in determining the specific domain shapes observed during the growth of Bi_2Se_3 .

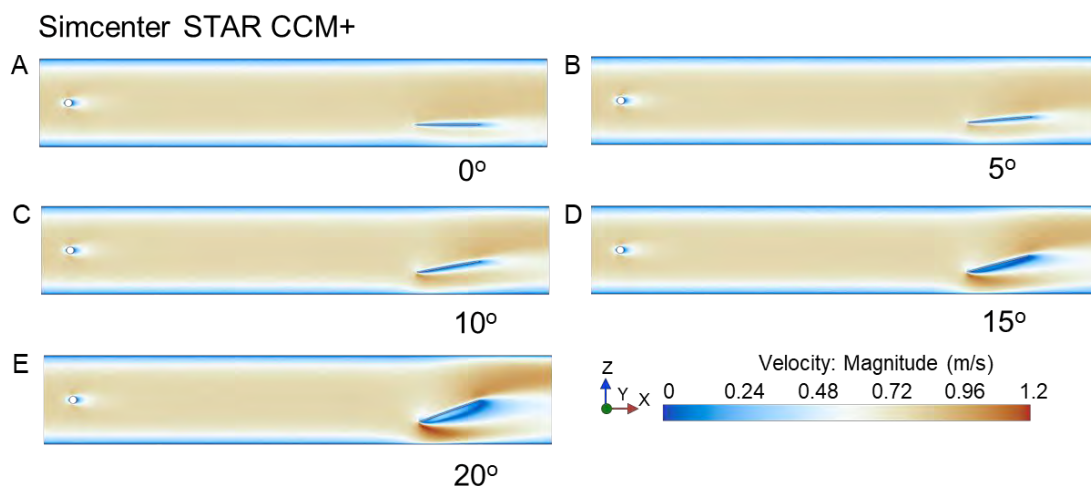


Figure S10. Simulations of carrier gas velocity. (A-E) Simulated distribution of carrier gas velocity using Simcenter STAR CCM+ software for the CVD systems with a solution time of 17.17 s and distinct titled angles of mica substrates, including 0°, 5°, 10°, 15°, and 20°, respectively. The quality, uniformity, and properties of the synthesized 2D materials via CVD are influenced by many factors, and the interplay between different factors, e.g., temperature, pressure, time, flow rate, etc., is complex in experiments. Among these factors, flow rate and precursor concentration stand out as particularly important, as they directly involve the reaction dynamics of vapor-phase precursors on a desired substrate.

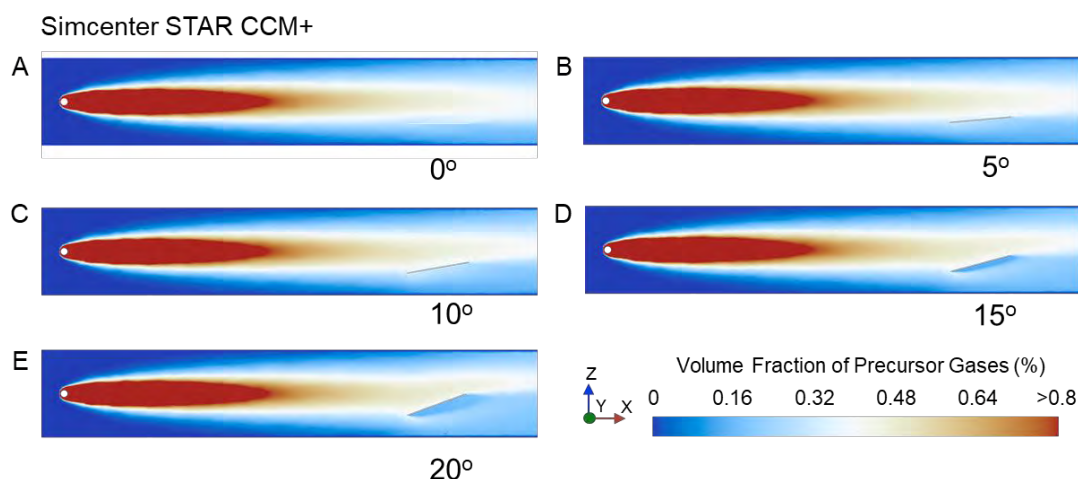


Figure S11. Simulations of precursor concentration diffusion. (A-E) Simulated precursor volume fraction of precursor gases (%) (precursor concentration) along the tube geometry at equilibrium with a solution time of 17.17 s and distinct titled angles of mica substrates, including 0°, 5°, 10°, 15°, and 20°, respectively.

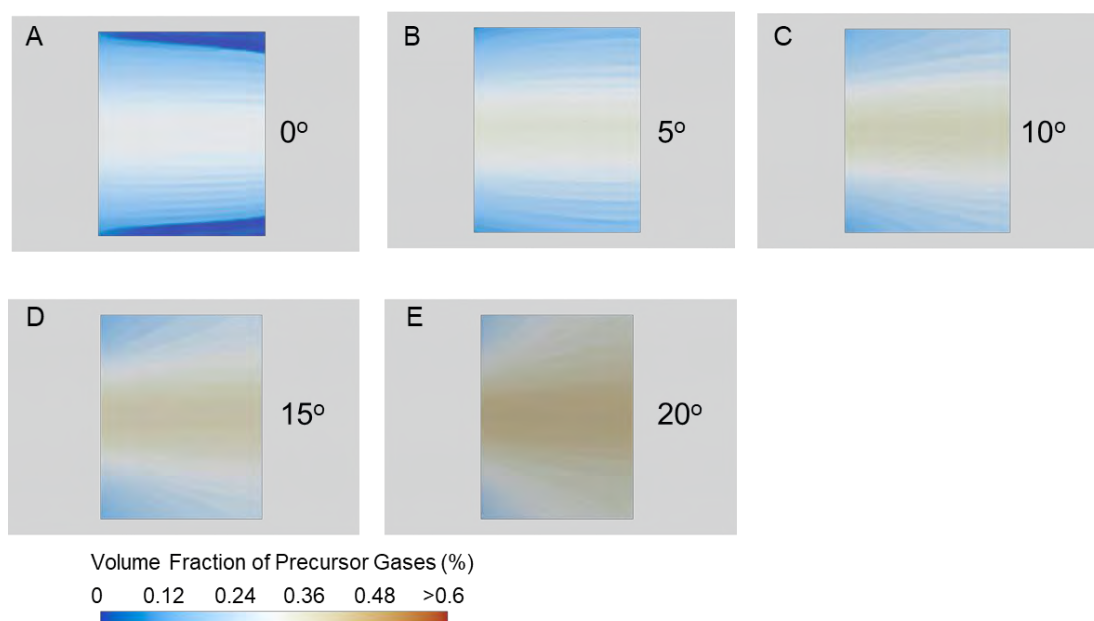


Figure S12. Simulated precursor concentration gradient. (A-E) Simulated precursor volume fraction of precursor gases (%) (precursor concentration) near the top surface of the mica substrate at equilibrium with a solution time of 17.17 s and distinct titled angles, including 0°, 5°, 10°, 15°, and 20°, respectively.

The synthesis of 2D materials through chemical vapor deposition (CVD) is a complex technique influenced by various factors, e.g., temperature, pressure, time, flow rate, precursor concentration, etc., which determines the quality, uniformity, and properties of the synthesized 2D materials. Among these factors, the flow rate and precursor concentration are particularly crucial. In CVD systems, the carrier gas and precursor vapor dynamics within the reactor can create concentration and deposition rate gradients across the substrate, impacting the uniformity and quality of the synthesized 2D material. By combining hydrodynamic modeling with concentration-diffusion modeling (Figure S10-12), these simulations allowed us to examine the relationship between flow rate and precursor concentration for different titled angles of the mica substrate. Our findings reveal that as the titled angle of the mica substrate increases from 0° to 20°, the flow rate across the growth substrate gradually increases (Figure S10). This enhanced flow rate boosts the feeding rate of precursors across the substrate, resulting in improved reaction dynamics of the vapor-phase precursors on the substrate. Furthermore, with the increase of the tilted angle, the precursor concentration keeps high uniformity on the proposed growth substrate with a lower precursor concentration dissipation (Figure S11-12), thereby ensuring superior control over the morphology and uniformity of the resulting films compared to conventional CVD methods. Notably, these results agree well with our experimental findings, providing strong evidence for the robust achievement of aligned growth in our study.

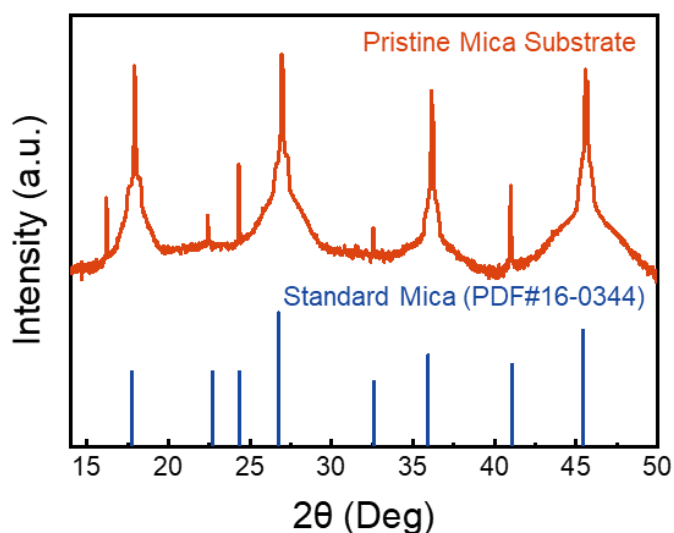


Figure S13. XRD tests of pristine mica substrate. The XRD patterns of the pristine mica substrate, closely matching the standard X-ray diffraction card (PDF No. 16-0344).

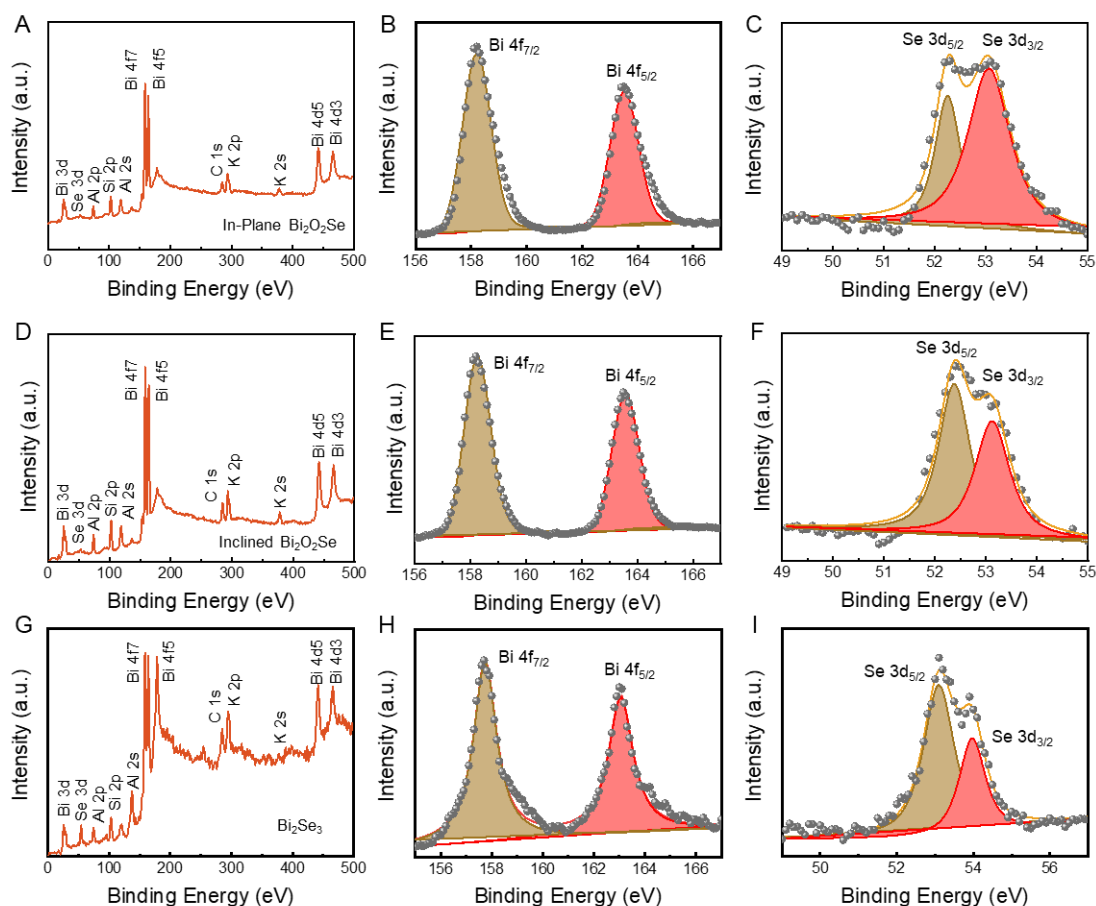


Figure S14. XPS analysis of distinct 2D products. (A-C) XPS spectra of few-layer in-plane $\text{Bi}_2\text{O}_2\text{Se}$ flakes on mica substrate, where Bi and Se peaks are resolved. The peaks of Bi are centered at 163.5 eV and 158.2 eV, corresponding to the binding energy of Bi 4f_{5/2} and Bi 4f_{7/2} (B), respectively. The spectrum of Se is resolved into two peaks, Se 3d_{5/2} and Se 3d_{3/2}, with the binding energy of 52.3 eV and 53.1 eV (C), respectively. (D-F) XPS spectra of inclined $\text{Bi}_2\text{O}_2\text{Se}$ flakes on mica substrate after ultrasonic treatment. No pronounced shift for Bi 4f (E) and Se 3d (F) is observed in contrast to the as-grown in-plane $\text{Bi}_2\text{O}_2\text{Se}$ flakes. (G-I) XPS spectra of as-grown few-layer Bi_2Se_3 flakes on mica substrate. XPS spectra of Bi 4f (H) with binding energy peaks at 163.1 and 157.7 eV are resolved, respectively. The spectrum of Se is resolved

into two peaks, Se 3d_{5/2} and Se 3d_{3/2}, with the binding energy of 53.1 eV and 53.9 eV (I), respectively. The XPS tests reveal the chemical bonding states of Bi and Se for Bi₂O₂Se and Bi₂Se₃, and all the resolved peaks are consistent with the composition of previous work.^{42,43}

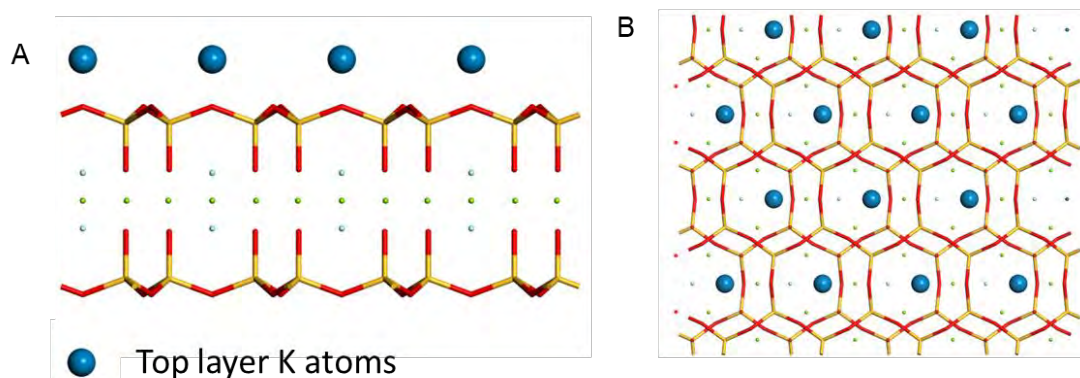


Figure S15. Atomic structures of mica substrate. (A) [110] projection of the muscovite mica structure, in which the top layer K atoms on mica {001} planes are manually enlarged to be more easily distinguished. (B) The basal plane [001] of the cleaved surface shows the hexagonal symmetry of the K⁺ layers.

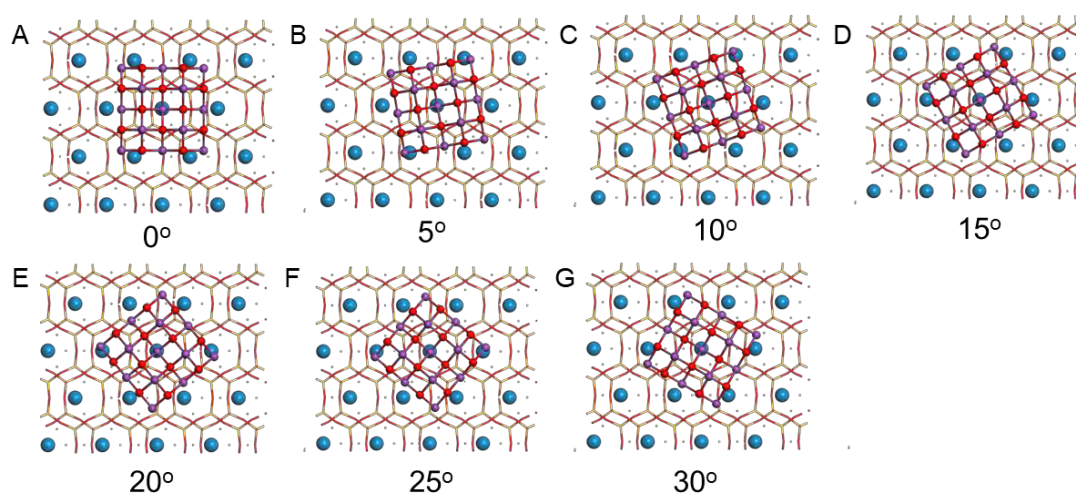


Figure S16. Atomic models for binding energy calculations. (A-G) Optimized structures for calculating the weak interaction between a tetragonal Bi₂O₂Se cluster and mica surface. The angle between the Bi₂O₂Se edge direction and the closely packed direction of K⁺ is given for each structure.

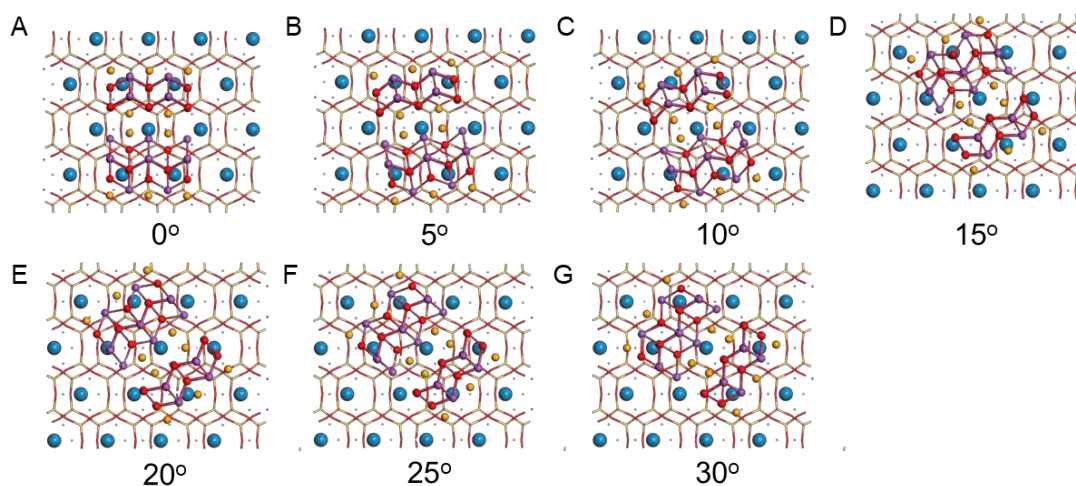


Figure S17. Atomic models for binding energy calculations. (A-G) Optimized structures for calculating the interaction between an inclined $\text{Bi}_2\text{O}_2\text{Se}$ cluster and mica surface. The angle between the inclined $\text{Bi}_2\text{O}_2\text{Se}$ edge direction and the closely packed direction of K^+ is given for each structure.

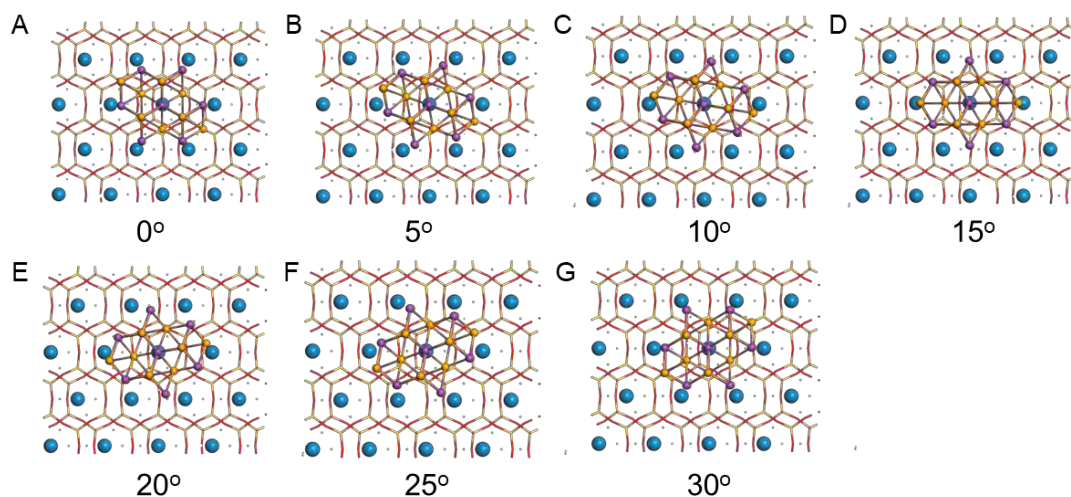


Figure S18. Atomic models for binding energy calculations. (A-G) Optimized structures for calculating the interaction between an inclined Bi_2Se_3 cluster and mica surface. The angle between the Bi_2Se_3 edge direction and the closely packed direction of K^+ is given for each structure.

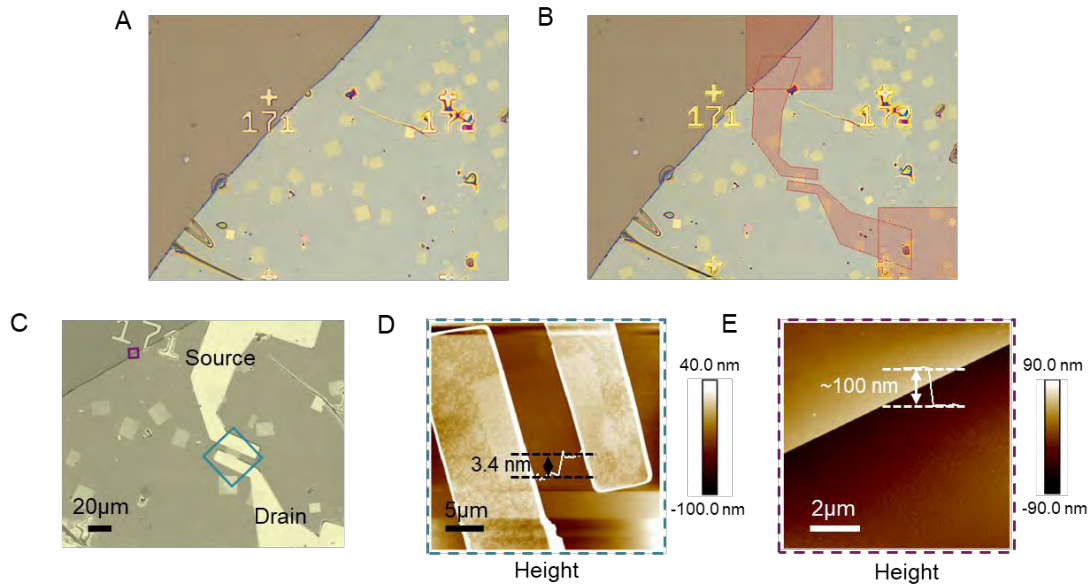


Figure S19. Fabrication of the desired 2D $\text{Bi}_2\text{O}_2\text{Se}$ FETs. (A) OM of the $\text{Bi}_2\text{O}_2\text{Se}/\text{Mica}$ transferred onto the 50 nm SiO_2/Si with marks, where exfoliated thin mica and SiO_2 layers serve as the hybrid dielectrics for $\text{Bi}_2\text{O}_2\text{Se}$ FETs. (B) Proposed electrodes drawn in the Layout Editor software before photolithography. (C) OM image of the device after a standard photolithography and electrode deposition process, where the $\text{Bi}_2\text{O}_2\text{Se}$ semiconductor and ultrathin exfoliated mica serve as the transistor channel and the insulator layer, respectively. (D-E) Thicknesses of the $\text{Bi}_2\text{O}_2\text{Se}$ channel and mica insulator characterized by atomic force microscopy (AFM), demonstrating that the thickness of the $\text{Bi}_2\text{O}_2\text{Se}$ layer is 3.4 nm and ~ 100 nm, respectively. The root-mean-square (RMS) roughness for the $\text{Bi}_2\text{O}_2\text{Se}$ surface and mica dielectric is calculated to be 6.14 Å and 6.41 Å within an area of $2 \times 2 \mu\text{m}$, exhibiting their atomic-scale flatness, respectively.

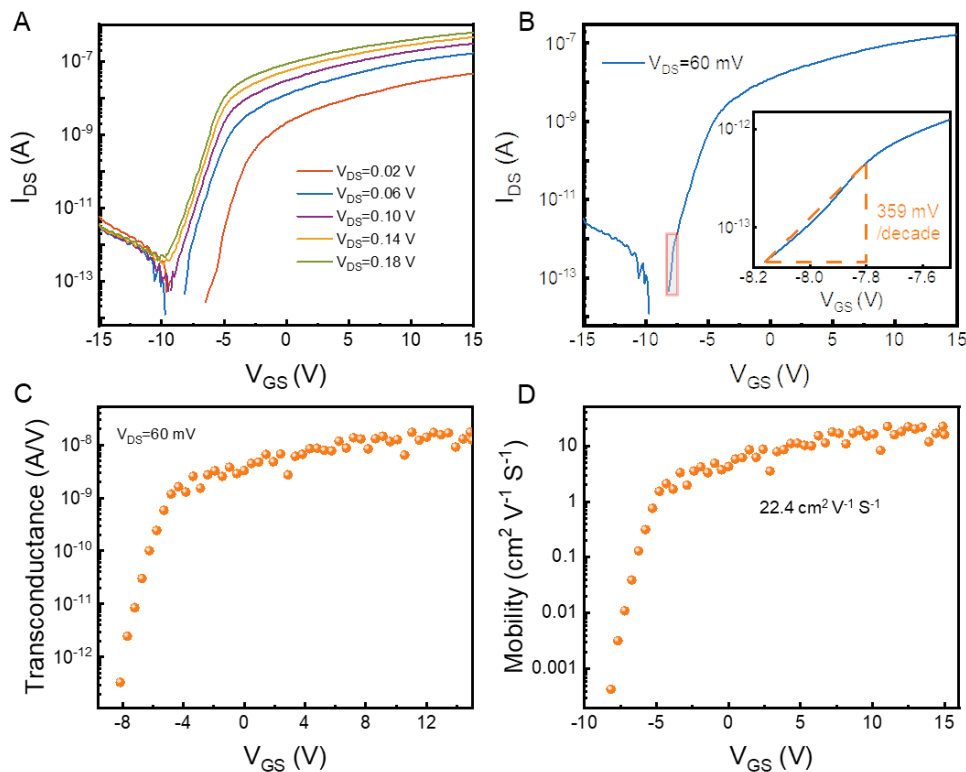


Figure S20. Carrier mobility calculations of the device. (A) Transfer curves of the device on a logarithmic scale at distinct biases under gate sweep ± 15 V. (B) Transfer curve of the device at $V_{\text{DS}} = 60$ mV under gate sweep ± 15 V. The inset figure exhibits that the minimal subthreshold

swing (SS) of the device is around 359 mV/decade. (C-D) Transconductance and mobility calculation of the device using a hybrid dielectric gate (100 nm mica/ 50 nm SiO₂), respectively.

The FET device exhibits intriguing electric properties, e.g., a maximum on/off ratio over 10⁷ and high carrier mobility. ⁴⁴The room-temperature apparent field-effect mobility (μ) as a function of gate voltage (V_{GS}) can be estimated using the dI_{DS}/dV_{GS} differential based on the equation (1)³²

$$\mu = \frac{L}{W} \frac{1}{C_g} \frac{dI_{DS}}{V_{DS} dV_{GS}} \quad (1)$$

where C_g is the equivalent capacitance of the hybrid dielectric, and L and W are the channel length and width, respectively. Since the geometry of the capacitor containing a composite dielectric is discretized into two parallel-plate capacitor elements, 100 nm Mica and 50 nm SiO₂, the equivalent capacitance of the structure can be calculated by the equation (2)⁴⁵

$$\frac{1}{C_g} = \frac{1}{C_{Mica}} + \frac{1}{C_{SiO_2}} \quad (2)$$

where C_{Mica} and C_{SiO_2} are the oxide capacitance of the 100 nm mica and 50 nm SiO₂, respectively. According to the previous report, 100 nm muscovite mica and 50 nm SiO₂ capacitance are measured at 40 nFcm⁻² and 70.8 nFcm⁻², respectively.^{46,47} Thus, the equivalent capacitance of the hybrid dielectric is calculated to be 25.56 nFcm⁻². The mobility of Bi₂O₂Se flakes versus V_{GS} characteristics can be extracted at $V_{DS} = 60$ mV, exhibiting high electron mobility with $\mu = 22.4$ cm² V⁻¹ s⁻¹.

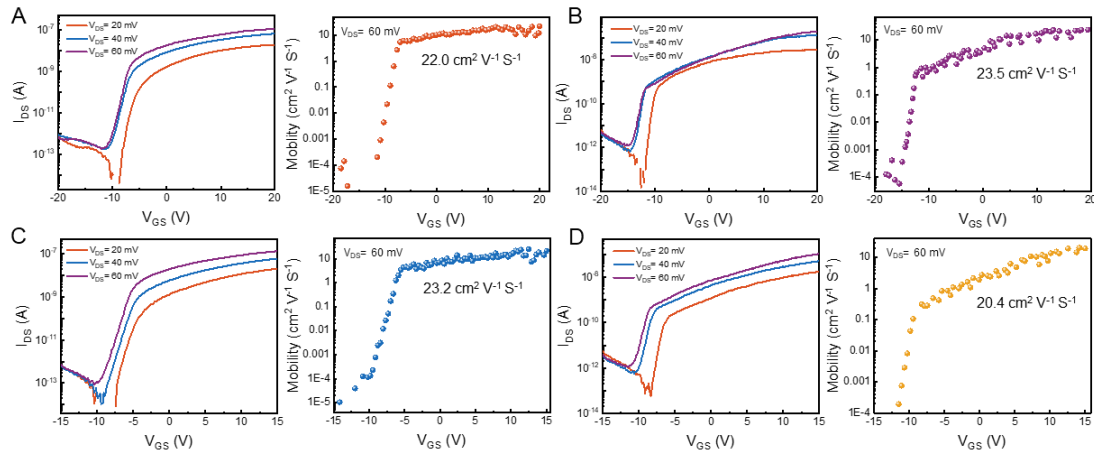


Figure S21. Statistical carrier mobility of ultrathin 2D Bi₂O₂Se. Mobility calculations of mica-based FETs directly using as-grown Bi₂O₂Se flakes as channel materials, in which the channel materials have a thickness of 3.2 nm (A), 3.1 nm (B), 3.5 nm (C), and 3.3 nm (D), respectively. The mean value and standard deviation of the mobility of the as-grown ultrathin 2D Bi₂O₂Se (≈ 6 layers, ~ 3.3 nm) are 22.3 and 1.2 cm² V⁻¹ S⁻¹, respectively.

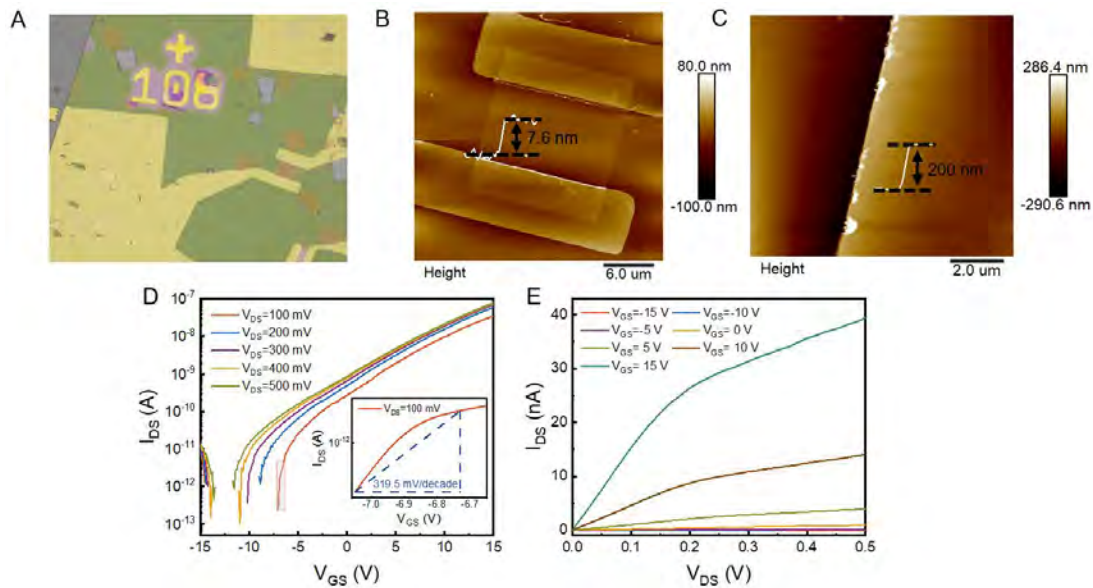


Figure S22. Performance of a $\text{Bi}_2\text{O}_2\text{Se}$ -channeled FET with mica dielectric. (A) Optical image of a back-gated $\text{Bi}_2\text{O}_2\text{Se}$ FET, in which $\text{Bi}_2\text{O}_2\text{Se}$ flakes with (B) a thickness of 7.6 nm serving as channel materials and (C) 200 nm mica as the dielectric layers. (D) Transfer curves of the device on a logarithmic scale at distinct V_{DS} under ± 15 V gate sweeping demonstrate a maximal current on/off ratio of $>10^6$ with an ultralow off current of about 0.1 pA. The inset figure shows the corresponding output curves at a small $V_{DS}=100$ mV, showing an excellent subthreshold swing of 319.5 mV decade $^{-1}$. (E) Output curves of the $\text{Bi}_2\text{O}_2\text{Se}$ FET using merely 200-nm mica as the dielectric layer under ± 15 V sweep voltages.

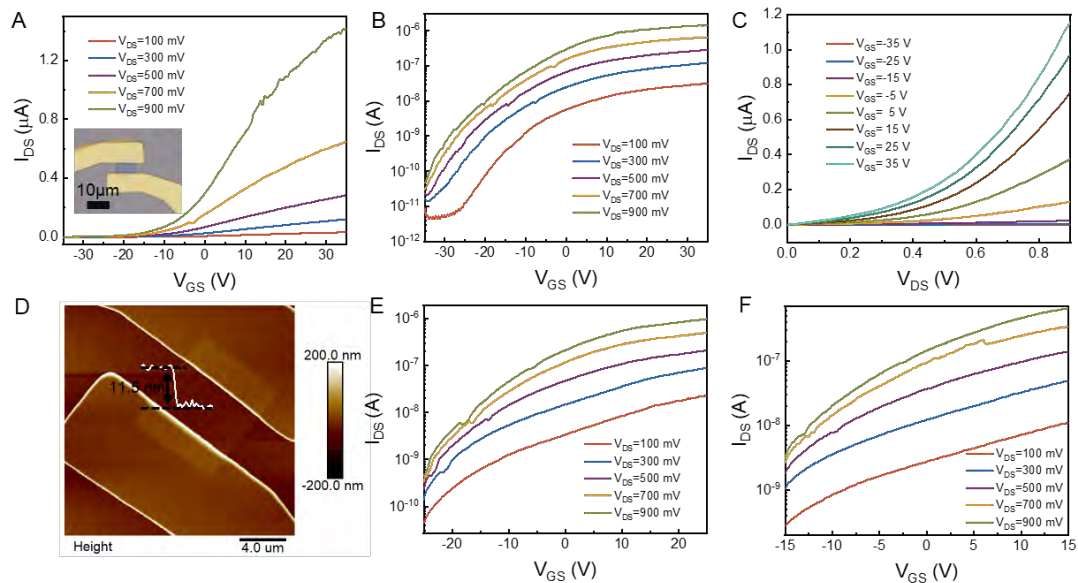


Figure S23. Performance of a FET with wet-transferred in-plane $\text{Bi}_2\text{O}_2\text{Se}$ channels. (A-B) Linear and related logarithmic transfer curves of the device on 50 nm SiO_2 at distinct biases under gate sweep ± 35 V, respectively. The inset figure shows the optical image of the FET using wet transferred $\text{Bi}_2\text{O}_2\text{Se}$ flake and 50nm SiO_2 as the channel material and gate dielectrics, in which the maximal current on/off ratio is merely 10^4 . This value is much lower than that of the device using as-grown $\text{Bi}_2\text{O}_2\text{Se}$ on mica as channel material, which could be attributed to disorder-induced performance degradation from the transfer process. (C) Corresponding output characteristics of the $\text{Bi}_2\text{O}_2\text{Se}$ FET under distinct gate sweep voltages. (D) AFM image of the $\text{Bi}_2\text{O}_2\text{Se}$ FET indicates the channel material thickness of 11.5 nm. (E-F) Transfer curves of the device at distinct gate sweep ranges, -25 - 25 V and -15 - 15 V, respectively.

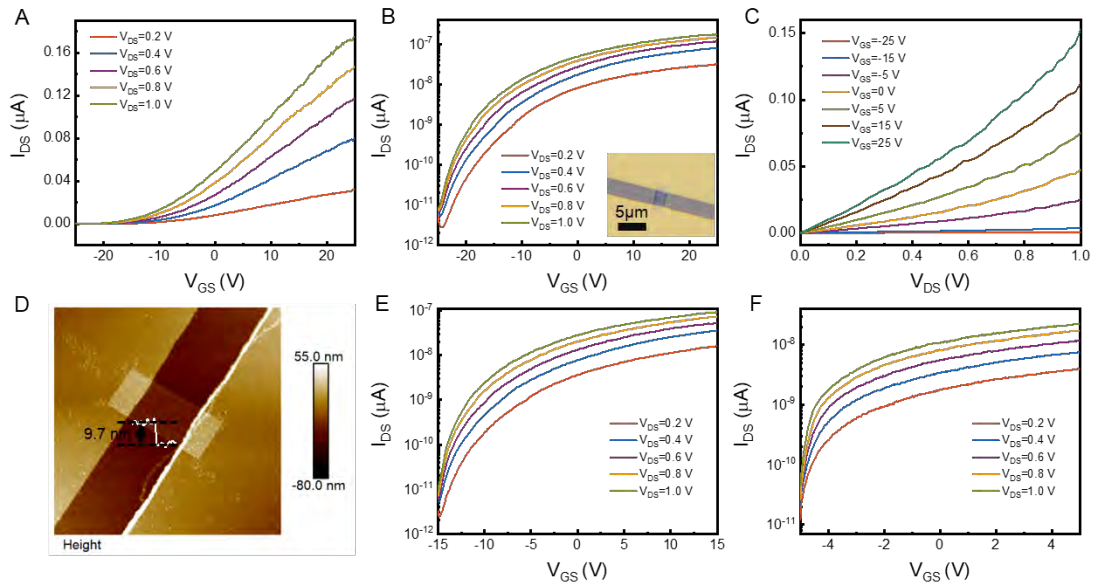


Figure S24. Performance of a FET with inclined $\text{Bi}_2\text{O}_2\text{Se}$ channels. (A-B) Linear and logarithmic transfer curves on 50 nm SiO_2 at distinct biases under gate sweep ± 35 V, respectively. The inset figure shows the optical image of the flatwise $\text{Bi}_2\text{O}_2\text{Se}$ FET using 50nm SiO_2 as the gate dielectrics, in which the maximal current on/off ratio is merely 10^4 , comparable to the device using wet-transferred $\text{Bi}_2\text{O}_2\text{Se}$ as the channel material. (C) Corresponding output characteristics of the $\text{Bi}_2\text{O}_2\text{Se}$ FET under distinct gate sweep voltages. (D) AFM image of the $\text{Bi}_2\text{O}_2\text{Se}$ FET indicates the channel material thickness of 11.5 nm. (E-F) Transfer curves of the device at distinct gate sweep ranges, -25-25 V and -15-15 V, respectively.

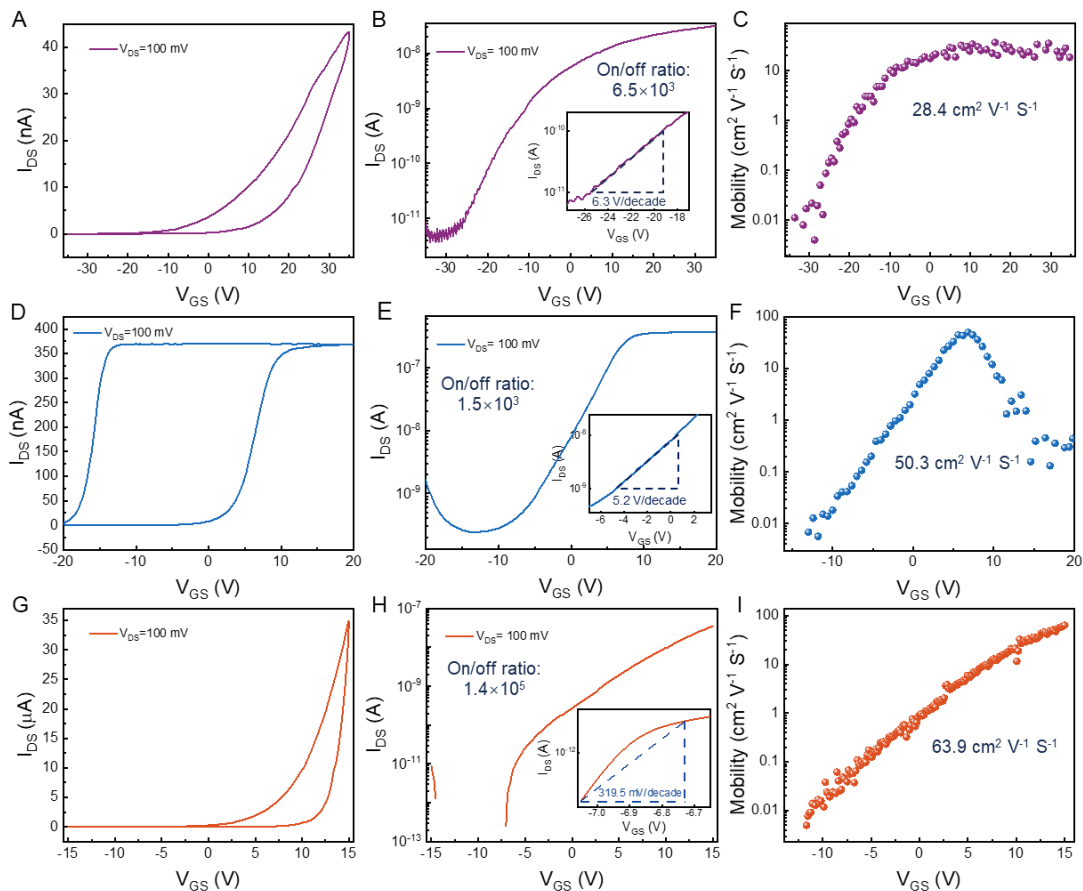


Figure S25 Performance comparison of the $\text{Bi}_2\text{O}_2\text{Se}$ FETs using different dielectric insulators. (A-C) Performance of back-gated $\text{Bi}_2\text{O}_2\text{Se}$ FET, in which wet-transferred $\text{Bi}_2\text{O}_2\text{Se}$

flake with a thickness of 7.9 nm serves as channel material and 50 nm SiO_2 as the dielectric layer. (D-F) Performance of top-gated $\text{Bi}_2\text{O}_2\text{Se}$ FET using 7.4nm thick $\text{Bi}_2\text{O}_2\text{Se}$ flake as channel material and 25nm Al_2O_3 as dielectric layer. (G-I) Performance of back-gated $\text{Bi}_2\text{O}_2\text{Se}$ FET directly using as-grown $\text{Bi}_2\text{O}_2\text{Se}$ flake (7.6 nm)/ mica (200 nm) as the dielectric layer.

Compared with the FETs using wet-transferred $\text{Bi}_2\text{O}_2\text{Se}$ or the FETs using vapor-deposited Al_2O_3 dielectric, the as-grown $\text{Bi}_2\text{O}_2\text{Se}$ transistor using original vdWs epitaxial dielectric exhibits higher electron mobility, larger current on/off ratio, and small subthreshold swing, showing its superiority in reducing the performance degradation of the CVD-grown 2D semiconductors. It is worth noting that the hysteresis observed in these devices encompasses both ferroelectric-induced and defect-induced hysteresis,⁴⁸ making it inappropriate to compare this key attribute among the devices directly.

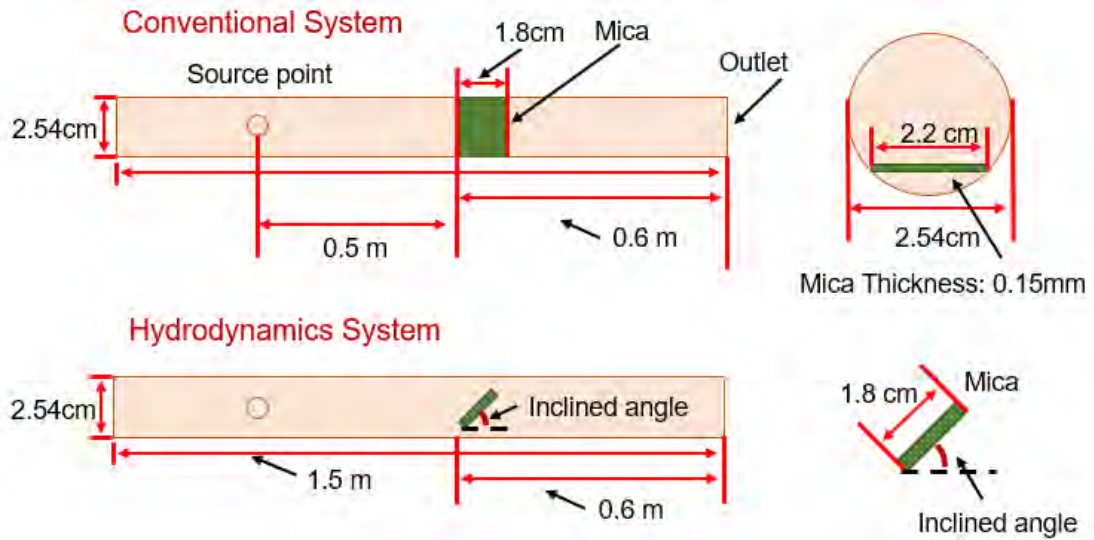


Figure S26. Model geometry for Simcenter STAR CCM+ simulation. Conventional system (Upper) and hydrodynamic system (Lower), respectively.

References

- [S1] Li, J., Wang, Z.X., Wen, Y., Chu, J.W., Yin, L., Cheng, R.Q., Lei, L., He, P., Jiang, C., Feng, L.P., and He, J. (2018). High-Performance Near-Infrared Photodetector Based on Ultrathin Bi₂O₂Se Nanosheets. *Adv. Funct. Mater.* **28**, 1706437. <https://doi.org/10.1002/adfm.201706437>.
- [S2] Chen, W., Zhang, R., Sun, Y., Wang, J., Fan, Y., and Liu, B. (2022). Preparation, properties, and electronic applications of 2D Bi₂O₂Se. *Advanced Powder Materials* **2**, 100080. <https://doi.org/10.1016/j.apmate.2022.100080>
- [S3] Hong, C.Y., Tao, Y., Nie, A.M., Zhang, M.H., Wang, N., Li, R.P., Huang, J.Q., Huang, Y.Q., Ren, X.M., Cheng, Y.C., and Liu, X.L. (2020). Inclined Ultrathin Bi₂O₂Se Films: A Building Block for Functional van der Waals Heterostructures. *ACS Nano* **14**, 16803-16812. <https://doi.org/10.1021/acsnano.0c05300>.
- [S4] Kong, D.S., Cha, J.J., Lai, K.J., Peng, H.L., Analytis, J.G., Meister, S., Chen, Y.L., Zhang, H.J., Fisher, I.R., Shen, Z.X., and Cui, Y. (2011). Rapid Surface Oxidation as a Source of Surface Degradation Factor for Bi₂Se₃. *ACS Nano* **5**, 4698-4703. <https://doi.org/10.1021/nn200556h>.
- [S5] Angel, R.J., Murri, M., Mihailova, B., and Alvaro, M. (2019). Stress, strain and Raman shifts. *Zeitschrift für Kristallographie-Crystalline Materials* **234**, 129-140. <https://doi.org/10.1515/zkri-2018-2112>
- [S6] Chen, S.S., Liu, H.T., Chen, F.H., Zhou, K., and Xue, Y.Z. (2020). Synthesis, Transfer, and Properties of Layered FeTe₂ Nanocrystals. *ACS Nano* **14**, 11473-11481. <https://doi.org/10.1021/acsnano.0c03863>.
- [S7] Liu, H.T., and Xue, Y.Z. (2021). Van Der Waals Epitaxial Growth and Phase Transition of Layered FeSe₂ Nanocrystals. *Adv. Mater.* **33**, 2008456. <https://doi.org/10.1002/adma.202008456>.
- [S8] Shi, J.P., Huan, Y.H., Zhao, X.X., Yang, P.F., Hong, M., Xie, C.Y., Pennycook, S., and Zhang, Y.F. (2021). Two-Dimensional Metallic Vanadium Ditelluride as a High-Performance Electrode Material. *ACS Nano* **15**, 1858-1868. <https://doi.org/10.1021/acsnano.0c10250>.
- [S9] Yang, F., Wong, M.-C., Mao, J., Wu, Z., and Hao, J. (2022). Synthesis and enhanced piezoelectric response of CVD-grown SnSe layered nanosheets for flexible nanogenerators. *Nano Research* **16**, 11839-11845. <https://doi.org/10.1007/s12274-022-5230-5>
- [S10] Zhao, S., Wang, H., Zhou, Y., Liao, L., Jiang, Y., Yang, X., Chen, G., Lin, M., Wang, Y., and Peng, H. (2015). Controlled synthesis of single-crystal SnSe nanoplates. *Nano research* **8**, 288-295. <https://doi.org/10.1007/s12274-014-0676-8>
- [S11] Liu, L.N., Wu, J.X., Wu, L.Y., Ye, M., Liu, X.Z., Wang, Q., Hou, S.Y., Lu, P.F., Sun, L.F., Zheng, J.Y., et al. (2018). Phase-selective synthesis of 1T-MoS₂ monolayers and heterophase bilayers. *Nat. Mater.* **17**, 1108. <https://doi.org/10.1038/s41563-018-0187-1>.
- [S12] Chen, M.R., Zhang, A.Y., Liu, Y.H., Cui, D.Z., Li, Z., Chung, Y.H., Mutyala, S.P., Mecklenburg, M., Nie, X., Xu, C., et al. (2020). Gold-vapor-assisted chemical vapor deposition of aligned monolayer WSe₂ with large domain size and fast growth rate. *Nano Research* **13**, 2625-2631. <https://doi.org/10.1007/s12274-020-2893-7>.
- [S13] Zhou, Y.B., Nie, Y.F., Liu, Y.J., Yan, K., Hong, J.H., Jin, C.H., Zhou, Y., Yin, J.B., Liu, Z.F., and Peng, H.L. (2014). Epitaxy and Photoresponse of Two-Dimensional GaSe Crystals on Flexible Transparent Mica Sheets. *ACS Nano* **8**, 1485-1490. <https://doi.org/10.1021/nn405529r>.
- [S14] Chang, H.C., Tu, C.L., Lin, K.I., Pu, J., Takenobu, T., Hsiao, C.N., and Chen, C.H. (2018). Synthesis of large - area InSe monolayers by chemical vapor deposition. *Small* **14**, 1802351. <https://doi.org/10.1002/smll.201802351>
- [S15] Zhang, Z., Zhao, B., Shen, D., Tao, Q., Li, B., Wu, R., Li, B., Yang, X., Li, J., and Song, R. (2021). Synthesis of ultrathin 2D nonlayered α - MnSe nanosheets, MnSe/WS₂ heterojunction for high - performance photodetectors. *Small Struct.* **2**, 2100028. <https://doi.org/10.1002/ssstr.202100028>
- [S16] Cui, F.F., Zhao, X.X., Xu, J.J., Tang, B., Shang, Q.Y., Shi, J.P., Huan, Y.H., Liao, J.H., Chen, Q., Hou, Y.L., et al. (2020). Controlled Growth and Thickness-Dependent Conduction-Type Transition of 2D Ferrimagnetic Cr₂S₃ Semiconductors. *Adv. Mater.* **32**, 1905896. <https://doi.org/10.1002/adma.201905896>.

- [S17] Wang, Y., Gan, L., Chen, J., Yang, R., and Zhai, T. (2017). Achieving highly uniform two-dimensional PbI₂ flakes for photodetectors via space confined physical vapor deposition. *Sci. Bull.* **62**, 1654-1662. <https://doi.org/10.1016/j.scib.2017.11.011>
- [S18] Chen, J., Fu, Y.P., Samad, L., Dang, L.N., Zhao, Y.Z., Shen, S.H., Guo, L.J., and Jin, S. (2017). Vapor-Phase Epitaxial Growth of Aligned Nanowire Networks of Cesium Lead Halide Perovskites (CsPbX₃, X = Cl, Br, I). *Nano Lett.* **17**, 460-466. <https://doi.org/10.1021/acs.nanolett.6b04450>.
- [S19] Chen, J., Luo, Z., Fu, Y., Wang, X., Czech, K.J., Shen, S., Guo, L., Wright, J.C., Pan, A., and Jin, S. (2019). Tin (IV)-tolerant vapor-phase growth and photophysical properties of aligned cesium tin halide perovskite (CsSnX₃; X= Br, I) nanowires. *ACS Energy Lett.* **4**, 1045-1052. <https://doi.org/10.1021/acseenergylett.9b00543>
- [S20] Wang, Z., Wang, P., Wang, F., Ye, J.F., He, T., Wu, F., Peng, M., Wu, P.S., Chen, Y.F., Zhong, F., et al. (2020). A Noble Metal Dichalcogenide for High-Performance Field-Effect Transistors and Broadband Photodetectors. *Adv. Funct. Mater.* **30**, 1907945. <https://doi.org/10.1002/adfm.201907945>.
- [S21] Fang, M.X., Wang, F., Han, Y.M., Feng, Y.L., Ren, T.L., Li, Y., Tang, D.X., Song, Z.T., and Zhang, K.L. (2018). Controlled Growth of Bilayer-MoS₂ Films and MoS₂-Based Field-Effect Transistor (FET) Performance Optimization. *Adv. Electron. Mater.* **4**, 1700524. <https://doi.org/10.1002/aelm.201700524>.
- [S22] Wang, L., Wang, X., Zhang, Y., Li, R., Ma, T., Leng, K., Chen, Z., Abdelwahab, I., and Loh, K.P. (2020). Exploring ferroelectric switching in α - In₂Se₃ for neuromorphic computing. *Adv. Funct. Mater.* **30**, 2004609. <https://doi.org/10.1002/adfm.202004609>
- [S23] Jiang, B., Zou, X.M., Su, J., Liang, J.H., Wang, J.L., Liu, H.J., Feng, L.P., Jiang, C.Z., Wang, F., He, J., and Liao, L. (2018). Impact of Thickness on Contact Issues for Pinning Effect in Black Phosphorus Field-Effect Transistors. *Adv. Funct. Mater.* **28**, 1801398. <https://doi.org/10.1002/adfm.201801398>.
- [S24] Wells, S.A., Henning, A., Gish, J.T., Sangwan, V.K., Lauhon, L.J., and Hersam, M.C. (2018). Suppressing Ambient Degradation of Exfoliated InSe Nanosheet Devices via Seeded Atomic Layer Deposition Encapsulation. *Nano Lett.* **18**, 7876-7882. <https://doi.org/10.1021/acs.nanolett.8b03689>.
- [S25] Wu, Z., Jiang, Z., Song, P., Tian, P., Hu, L., Liu, R., Fang, Z., Kang, J., and Zhang, T.Y. (2019). Nanowire - Seeded Growth of Single - Crystalline (010) β - Ga₂O₃ Nanosheets with High Field - Effect Electron Mobility and On/Off Current Ratio. *Small* **15**, 1900580. <https://doi.org/10.1002/smll.201900580>
- [S26] Ai, W., Chen, J.B., Dong, X.Y., Gao, Z.S., He, Y.Y., Liu, Z.C., Fu, H.X., Luo, F., and Wu, J.X. (2022). High Mobility and Quantum Oscillations in Semiconducting Bi₂O₂Te Nanosheets Grown by Chemical Vapor Deposition. *Nano Lett.* <https://doi.org/10.1021/acs.nanolett.2c02891>.
- [S27] Chubarov, M., Choudhury, T.H., Hickey, D.R., Bachu, S., Zhang, T.Y., Sebastian, A., Bansal, A., Zhu, H.Y., Trainor, N., Das, S., et al. (2021). Wafer-Scale Epitaxial Growth of Unidirectional WS₂ Monolayers on Sapphire. *ACS Nano* **15**, 2532-2541. <https://doi.org/10.1021/acsnano.0c06750>.
- [S28] Fu, Q.D., Zhu, C., Zhao, X.X., Wang, X.L., Chaturvedi, A., Zhu, C., Wang, X.W., Zeng, Q.S., Zhou, J.D., Liu, F.C., et al. (2019). Ultrasensitive 2D Bi₂O₂Se Phototransistors on Silicon Substrates. *Adv. Mater.* **31**, 1804945. <https://doi.org/10.1002/adma.201804945>.
- [S29] Zhang, C.C., Wu, J.X., Sun, Y.W., Tan, C.W., Li, T.R., Tu, T., Zhang, Y.C., Liang, Y., Zhou, X.H., Gao, P., and Peng, H.L. (2020). High-Mobility Flexible Oxyselenide Thin-Film Transistors Prepared by a Solution-Assisted Method. *J. Am. Chem. Soc.* **142**, 2726-2731. <https://doi.org/10.1021/jacs.9b11668>.
- [S30] Tan, C.W., Tang, M., Wu, J.X., Liu, Y.N., Li, T.R., Liang, Y., Deng, B., Tan, Z.J., Tu, T., Zhang, Y.C., et al. (2019). Wafer-Scale Growth of Single-Crystal 2D Semiconductor on Perovskite Oxides for High-Performance Transistors. *Nano Lett.* **19**, 2148-2153. <https://doi.org/10.1021/acs.nanolett.9b00381>.
- [S31] Li, T., Tu, T., Sun, Y., Fu, H., Yu, J., Xing, L., Wang, Z., Wang, H., Jia, R., and Wu, J. (2020). A native oxide high-k gate dielectric for two-dimensional electronics. *Nat Electron.* **3**, 473-478. <https://doi.org/10.1038/s41928-020-0444-6>
- [S32] Wu, J.X., Yuan, H.T., Meng, M.M., Chen, C., Sun, Y., Chen, Z.Y., Dang, W.H., Tan, C.W., Liu, Y.J., Yin, J.B., et al. (2017). High electron mobility and quantum oscillations in non-encapsulated ultrathin semiconducting Bi₂O₂Se. *Nat. Nanotechnol.* **12**, 530. <https://doi.org/10.1038/Nnano.2017.43>.

- [S33] Wang, H., Xu, X.Z., Li, J.Y., Lin, L., Sun, L.Z., Sun, X., Zhao, S.L., Tan, C.W., Chen, C., Dang, W.H., et al. (2016). Surface Monocrystallization of Copper Foil for Fast Growth of Large Single-Crystal Graphene under Free Molecular Flow. *Adv. Mater.* **28**, 8968-8974. <https://doi.org/10.1002/adma.201603579>.
- [S34] Wang, S.S., Rong, Y.M., Fan, Y., Pacios, M., Bhaskaran, H., He, K., and Warner, J.H. (2014). Shape Evolution of Monolayer MoS₂ Crystals Grown by Chemical Vapor Deposition. *Chem. Mater.* **26**, 6371-6379. <https://doi.org/10.1021/cm5025662>.
- [S35] Wang, J.W., Cai, X.B., Shi, R., Wu, Z.F., Wang, W.J., Long, G., Tang, Y.J., Cai, N.D., Ouyang, W.K., Geng, P., et al. (2018). Twin Defect Derived Growth of Atomically Thin MoS₂ Dendrites. *ACS Nano* **12**, 635-643. <https://doi.org/10.1021/acsnano.7b07693>.
- [S36] Cai, Z., Liu, B., Zou, X., and Cheng, H.-M. (2018). Chemical vapor deposition growth and applications of two-dimensional materials and their heterostructures. *Chem. Rev.* **118**, 6091-6133. <https://doi.org/10.1021/acs.chemrev.7b00536>.
- [S37] Wang, Q., Wang, S., Li, J.Y., Gan, Y.C., Jin, M.T., Shi, R., Amini, A., Wang, N., and Cheng, C. (2023). Modified Spatially Confined Strategy Enabled Mild Growth Kinetics for Facile Growth Management of Atomically-Thin Tungsten Disulfides. *Adv. Sci.* **10**. <https://doi.org/10.1002/advs.202205638>.
- [S38] Pierson, H.O. (1999). *Handbook of chemical vapor deposition: principles, technology and applications* (William Andrew).
- [S39] Gao, J., Lu, F.C., Liu, X.L., Deng, J.J., Zhang, X.Y., Sun, Z.H., Liu, X.C., Shi, X.J., Wang, N., Wu, Y.T., et al. (2022). Detection and tuning of spin-orbit interactions on inclined-grown Bi₂O₂Se nanoplates. *Appl. Phys. Lett.* **120**, 013105. <https://doi.org/10.1063/5.0072201>.
- [S40] Sunagawa, I. (1999). Growth and morphology of crystals. *FORMA-TOKYO-* **14**, 147-166.
- [S41] Tay, R.Y., Park, H.J., Ryu, G.H., Tan, D.L., Tsang, S.H., Li, H.L., Liu, W.W., Teo, E.H.T., Lee, Z., Lifshitz, Y., and Ruoff, R.S. (2016). Synthesis of aligned symmetrical multifaceted monolayer hexagonal boron nitride single crystals on resolidified copper. *Nanoscale* **8**, 2434-2444. <https://doi.org/10.1039/c5nr08036c>.
- [S42] Messalea, K.A., Zavabeti, A., Mohiuddin, M., Syed, N., Jannat, A., Atkin, P., Ahmed, T., Walia, S., McConville, C.F., and Kalantar - Zadeh, K. (2020). Two - Step Synthesis of Large - Area 2D Bi₂S₃ Nanosheets Featuring High In - Plane Anisotropy. *Adv. Mater. Interfaces* **7**, 2001131. <https://doi.org/10.1002/admi.202001131>
- [S43] Khan, U., Nairan, A., Khan, K., Li, S., Liu, B.L., and Gao, J.K. (2022). Salt-Assisted Low-Temperature Growth of 2D Bi₂O₂Se with Controlled Thickness for Electronics. *Small* **19**, 2206648. <https://doi.org/10.1002/smll.202206648>.
- [S44] Si, M.W., Saha, A.K., Gao, S.J., Qiu, G., Qin, J.K., Duan, Y.Q., Jian, J., Niu, C., Wang, H.Y., Wu, W.Z., et al. (2019). A ferroelectric semiconductor field-effect transistor. *Nat. Electron.* **2**, 580-586. <https://doi.org/10.1038/s41928-019-0338-7>.
- [S45] Patil, S.K., Koledintseva, M.Y., Schwartz, R.W., and Huebner, W. (2008). Prediction of effective permittivity of diphasic dielectrics using an equivalent capacitance model. *J. Appl. Phys.* **104**, 074108. <https://doi.org/10.1063/1.2976173>.
- [S46] He, Y.D., Dong, H.L., Meng, Q., Jiang, L., Shao, W., He, L.F., and Hu, W.P. (2011). Mica, a Potential Two-Dimensional-Crystal Gate Insulator for Organic Field-Effect Transistors. *Adv. Mater.* **23**, 5502. <https://doi.org/10.1002/adma.201103592>.
- [S47] Wang, W., Yip, S., Meng, Y., Wang, W., Wang, F., Bu, X., Lai, Z., Kang, X., Xie, P., and Quan, Q. (2021). Antimony - Rich GaAs_xSb_{1-x} Nanowires Passivated by Organic Sulfides for High - Performance Transistors and Near - Infrared Photodetectors. *Adv. Opt. Mater.* **9**, 2101289.
- [S48] Wang, W.J., Meng, Y., Zhang, Y.X., Zhang, Z.M., Wang, W., Lai, Z.X., Xie, P.S., Li, D.J., Chen, D., Quan, Q., et al. (2023). Electrically Switchable Polarization in Bi₂O₂Se Ferroelectric Semiconductors. *Adv. Mater.* **35**, 2210854. <https://doi.org/10.1002/adma.202210854>.